11-2014

Incoherent Scatter Radar Observations of Dynamic Ion Composition Changes at High Latitudes during Geomagnetic Storms

Bryan C. Wright
Embry-Riddle Aeronautical University - Daytona Beach

INCOHERENT SCATTER RADAR OBSERVATIONS OF DYNAMIC ION COMPOSITION CHANGES AT HIGH LATITUDES DURING GEOMAGNETIC STORMS

BY
BRYAN C. WRIGHT

A Thesis
Submitted to the Department of Physical Sciences
and the Committee on Graduate Studies
In partial fulfillment of the requirements
for the degree of
Master in Science in Engineering Physics

11/2014
Embry-Riddle Aeronautical University
Daytona Beach, Florida

INCOHERENT SCATTER RADAR OBSERVATIONS OF DYNAMIC ION COMPOSITION CHANGES AT HIGH LATITUDES DURING GEOMAGNETIC STORMS

by

Bryan C. Wright

This thesis was prepared under the direction of the candidate's Thesis Committee Chair, Dr. Matthew Zettergren, Assistant Professor, Daytona Beach Campus, and Thesis Committee Members Dr. John Hughes, Associate Professor, Daytona Beach Campus, and Dr. Jonathan Snively, Assistant Professor, Daytona Beach Campus, and has been approved by the Thesis Committee. It was submitted to the Department of Physical Sciences in partial fulfillment of the requirements for the degree of

Master of Science in Engineering Physics

THESIS COMMITTEE:

Dr. Matthew Zettergren,
Committee Chair

Dr. John Hughes,
Committee Member

Dr. Jonathan Snively,
Committee Member

Dr. Peter Erdman,
Graduated Program Chair,
Engineering Physics

Dr. Terry Oswalt,
Department Chair,
Physical Sciences

Dr. William Grams,
Dean, College of Arts and Sciences

Dr. Robert Oxley,
Associate V.P. for Academics

12-5-14

Abstract

Two new methods are developed for estimating F region ion composition from field-aligned incoherent scatter radar (ISR) measurements. These methods address incoherent scatter spectra temperature-mass ambiguities by self-consistently modeling ion temperature profiles as a function of electric fields and plasma interactions with the neutral atmosphere. These two new methods improve on previous, similar work developed in Zettergren et al. [2010,2011] by incorporating more accurate physical models and improving the estimation procedures. These techniques enable studies of ionospheric composition during highly disturbed conditions and are suitable for data collected with short integration times (2-10 minutes). The improved models incorporate the effects of variable scale height, altitude dependent neutral winds (taken from the horizontal wind model 2007), and Coulomb collisions, while the fitting schemes simultaneously determine both electric fields and features of composition. These new estimators are used to analyze Sondrestrom ISR datasets from 1998-2008 for quiet (Kp < 3) and storm (Kp > 3) times. Results are validated against previous observations of ionospheric composition, in particular, showing consistency with quiet time crossover altitude (the altitude where $n_{O^+} = n_{NO^+}$) diurnal trends, LT minimum and maximum, geomagnetic activity trends, and F region molecular ion increases due to frictional heating. Other results include rather large increases of F region molecular ion concentrations after sunrise during storms, a quantitative analysis of the crossover altitude dependence on effective electric field, and several observations of sudden composition variations in response to rapid Kp transitions. These methods are an improvement to existing approaches to fitting ISR data for ion composition, are applicable at high latitudes and during disturbed conditions, and illustrate several interesting features of how molecular ions respond to electric fields and geomagnetic activity.

Acknowledgments

This thesis has been possible through the support of my advisor, Dr. Matthew Zettergren. He is responsible for getting me interested in space physics and electricity & magnetism while encouraging a method and pace of learning well suited to myself. Thus, thank you. Thank you to Dr. John Hughes and Dr. Jonathan Snively for providing valuable feedback during the writing process. Thank you to all of the Physical Sciences Department, especially Susan Adams and Donna Fremont, for providing a fun learning environment where I gained a love for physics. Thanks to Anthony Pritchard for taking on the degrees' challenges with me throughout our time at ERAU. A big thank you to my family for always being there and giving their support and believing in me. A huge thank you to my fiancée, Sarah Rose, for always giving encouragement, keeping me focused, and being there to talk about anything.

Contents

Abstract **iv**

Acknowledgments **v**

1 Introduction **1**

1.1 Scientific Background 1

1.2 Outline of Thesis 4

2 Methodology **5**

2.1 Model Fitting 5

2.2 Model A 8

2.3 Model B 9

2.4 Model C 14

2.4.1 Collision Effects on Temperature 24

2.5 Recap: Procedure of Estimation 27

2.6 Error Checking: Determination of Bad Fits 27

3 Results: Case Studies at Sondrestrom **28**

3.1 Temperature Profile Examples 29

3.2 Neutral Wind Effects, Parameter Estimation, and 11 November 2003 Case Study 44

3.3 27 May 2003 Storm Case Study & 23 March 2006 Quiet Case Study . 50

3.3.1 Quiet versus Storm Variations 50

4 Results: Statistical Analysis of Case Studies **55**
4.1 Local Time Binning 55
4.1.1 Crossover Altitude 55
4.1.2 Effective Electric Field 57
4.1.3 Scale Height 58
4.1.4 Model Comparison 59
4.2 Local Time and Kp Binning 59
4.2.1 Model A 59
4.2.2 Model B 61
4.2.3 Model C 62
4.3 Transition Altitude Increases Due to Frictional Heating 66
4.4 Geomagnetic Activity Rapid Transitions and Crossover Altitude Disturbances 67
4.5 Summary of Average Results 69

5 Conclusions and Future Work **71**
5.1 Conclusions 71
5.2 Limitations and Future Work 73

List of Tables

3.1 The storm and quiet datasets used in this study. There are 11 storm datasets and 16 quiet datasets. 29

4.1 The average values of $\boldsymbol{x}_{est}$ for each Model for different geomagnetic conditions. NS, S, and ES, stand for near storm, storm, and extreme storm, respectively, as defined in Section 4.2. H averages do not include Model A as it assumed constant at 30 km. Quiet and Storm averages include all 3 models. 70

List of Figures

1.1 Sondrestrom ISR temperature inversion examples. Images courtesy of Zettergren et al. [2010]. 2

2.1 The effects of scale height and crossover altitude on ion parameterization. 11
2.2 Wind field given by HWM for 12 November 2003 midnight UT at Sondrestrom. 13
2.3 Wind field given by HWM for 28 August 1998 noon UT at Sondrestrom. 13
2.4 Electric field and electron temperature dependencies of ion temperatures. The electric field values for the bottom two plots are 50 $^{\mathrm{mV}}/_{\mathrm{m}}$. 25
2.5 The solution of the pressure tensor gives the parallel and perpendicular ion species temperatures as seen above for various electric field values. 26

3.1 A calm time period for 28 February 2008 at 1:08.84 UT. All models fit the data well up to 350 km where the radar temperature errors become large. Model A estimates the largest z_c. 33
3.2 A calm time period for 28 February 2008 at 3:00.72 UT. Models B and C fit the data extremely well with very similar parameters. Model C unnecessarily increases z_c and $E'_\perp$, and thus the temperature. 34
3.3 A heating event for 10 March 1998 at 11:34.44 UT. 35
3.4 A heating event for 10 March 1998 at 11:35.46 UT. 36
3.5 A heating event for 10 March 1998 at 11:42.54 UT. 37

3.6 A heating event for 10 March 1998 at 11:43.56 UT. 38
3.7 A heating event for 7 October 2002 at 00:30.55 UT. 39
3.8 A heating event for 7 October 2002 at 2:16.16 UT. 40
3.9 A heating event for 10 March 1998 at 11:47.64 UT. Models A and B both fit the radar data well, however Model B gives significantly lower estimates for z_c and $E'_\perp$. Model C gives an example of a bad fit as H and z_c hit the fitter rails as described in Section 2.6. 41
3.10 A heating event for 10 March 1998 at 11:51.72 UT. Model A fits the radar data but with large quantities of high altitude NO^+. Model B and C both meet the bad fit criteria as described in Section 2.6. 42
3.11 A heating event for 10 March 1998 at 11:54.78 UT. Models A and C both fit the data well while estimating very large z_c's. However, Model C fits the radar data better above 250 km which is where collisions start to make a large difference as seen in Figure 2.4. Model B gives an example of a bad fit as described in Section 2.6. 43
3.12 Model A and Model B, with and without explicit inclusion of neutral winds, for the 11 November 2003 storm dataset are juxtaposed along with geomagnetic activity. The vertical black lines indicate 6:30 am LT. 47
3.13 The correlation between effective electric field and crossover altitude for the data in Figure 3.12 above. 48
3.14 A heating event for 10 March 1998 at 11:34.44 UT. Models A and B are compared when they both implicitly estimate $\boldsymbol{u}_\perp \times \boldsymbol{B}$ by letting $u_\perp = 0$ for Model B. All parameters are lower for Model B which simultaneously estimates the parameters. See also Figure 3.3. 49
3.15 Models A, B, and C for the 27 May 2003 storm dataset are juxtaposed along with geomagnetic and neutral wind activity. 51
3.16 The correlation between effective electric field and crossover altitude for the data in Figure 3.15 above. 52
3.17 Models A, B, and C for the 23 March 2006 quiet dataset are juxtaposed along with geomagnetic and neutral wind activity. 53

3.18 The correlation between effective electric field and crossover altitude for the data in Figure 3.17 above. 54

4.1 The composition parameters, z_c, H, and $E'_\perp$, for Models A, B, and C, binned by local time. Model A is black, Model B is blue, and Model C is red. Storm data is on the left while quiet data is on the right. . . 56
4.2 Model A's crossover altitude at local times binned into K_p index. The disturbed panels ($K_p \geq 3$)show a z_c enhancement from 20 to 15 LT as compared to the quiet panel ($K_p < 3$). 60
4.3 Model A's effective electric field at local times binned into K_p index. The disturbed panels ($K_p \geq 3$) show an $E'_\perp$ enhancement from nightfall to noon. The average in the panels from left to right are roughly 20, 30, and 40 $^{mV}/_{m}$. 63
4.4 Model B's crossover altitude at local times binned into K_p index. The disturbed panels ($K_p \geq 3$) show a z_c enhancement as compared to the quiet panel ($K_p < 3$). 63
4.5 Model B's scale height at local times binned into K_p index. The disturbed panels ($K_p \geq 3$) show an overall H enhancement as compared to the quiet panel ($K_p < 3$) with peaks at nighttime. 64
4.6 Model B's electric and effective electric field at local times binned into K_p index. The disturbed panels ($K_p \geq 3$) show an $E'_\perp$ enhancement from nightfall to noon. The average in the panels from left to right are roughly 20, 25, and 35 $^{mV}/_{m}$. 64
4.7 Model C's crossover altitude at local times binned into K_p index. The disturbed panels ($K_p \geq 3$) show a z_c enhancement as compared to the quiet panel ($K_p < 3$). 64
4.8 Model C's scale height at local times binned into K_p index. The disturbed panels($K_p \geq 3$) show an overall H enhancement as compared to the quiet panel ($K_p < 3$) with peaks at nighttime. 65

4.9 Model C's electric and effective electric field at local times binned into K_p index. The disturbed panels ($K_p \geq 3$) show an $E'_\perp$ enhancement from nightfall to noon. The average in the panels from left to right are roughly 25, 30, and 40 $^{mV}/_{m}$. 65
4.10 The effect of the effective electric field on crossover altitude for quiet and storm datasets. 67
4.11 K_p and z_c throughout the storm of 27 May 2003. There is a large amount of z_c variation near large K_p transitions. 68
4.12 K_p and z_c throughout the storm of 11 November 2003. There is a large amount of z_c variation near large K_p transitions. 69

Chapter 1

Introduction

1.1 Scientific Background

Incoherent scatter radar (ISR) techniques have been used since the 1960s in order to learn more about our atmosphere. ISR instruments allow for a long time history (hours to days) of plasma parameters such as ion and electron temperature, density, and velocity data to be collected. These data discern a clear dependence on local time, latitude, longitude, and altitude [Evans, 1969]. Parameters are found by fitting the IS spectra to a theoretical model from which are extracted the ion temperature to mass ratio (T_i/m_i), the electron temperature to ion temperature ratio (T_e/T_i), the ion line-of-sight drift velocity (v_i), and the electron density (n_e) [Farley, 1969, Dougherty and Farley, 1960, Hagfors, 1961, Moorcroft, 1964, Waldteufel, 1971, Evans, 1969]. Computation of absolute ion and electron temperatures from the IS spectrum requires assumptions about the O^+ and NO^+ densities [Evans, 1969, Oliver, 1979, Lathuillere et al., 1983, Waldteufel, 1971]. This ion composition is often assumed to be static when processing IS spectra, such as at the Sonderstrom ISR facility (where the data for this work's test cases come from). In the high latitude ionosphere, this often leads to unphysical temperature profiles [Zettergren et al., 2010, and references therein]. An example of an unphysical temperature is given in Figure 1.1a. These inversions are seen in the F1 region and show vast

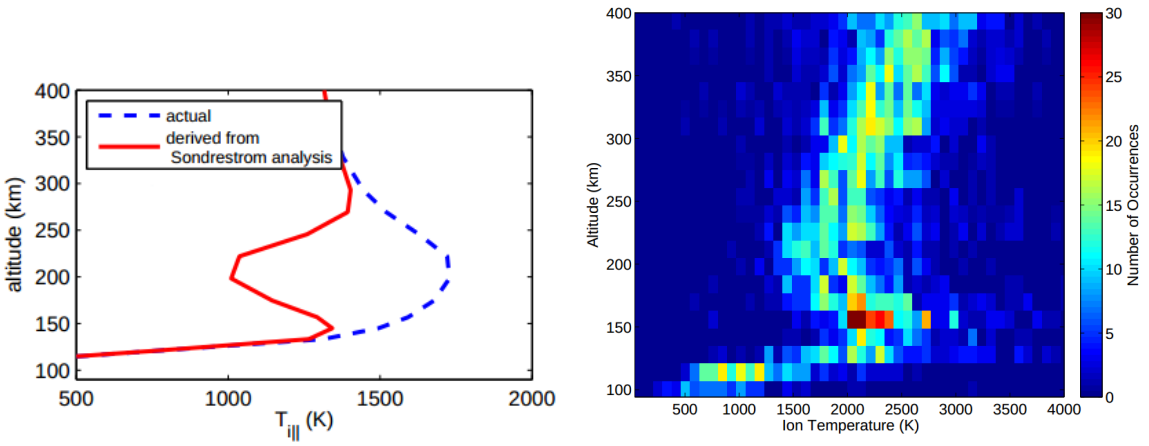

(a) Inversion Profile (b) Inversion Histogram

Figure 1.1: Sondrestrom ISR temperature inversion examples. Images courtesy of Zettergren et al. [2010].

temperature differences (500-1000 K) compared to modeled temperatures [Zettergren et al., 2010]. It is noted that these inversions are common, as seen in Figure 1.1b, which shows a histogram of occurrences of temperature values at various altitudes.

Ionospheric temperatures are driven by frictional heating due to $\boldsymbol{E}_\perp \times \boldsymbol{B}$ ion drift through the neutral atmosphere. However, high latitude ionosphere ion composition is easily altered by the highly temperature sensitive reaction

$$O^+ + N_2 \rightarrow NO^+ + N \tag{1.1}$$

which favors conversion of O^+ to NO^+ at a rate roughly proportional to T^2 [McFarland et al., 1973, Torr et al., 1977, Saint Maurice and Torr, 1978, St.-Maurice and Laneville, 1998]. Thus, incorrect temperatures will be derived from the IS spectra when there are heating events, due to incorrect ion composition assumptions via Equation (1.1) constantly altering the ion composition.

In order to address these temperature inversions, ion composition variability in the ionosphere has been modeled in Schunk et al. [1975], Diloy et al. [1996], Zettergren et al. [2010, 2011] but has not been definitively accounted for in the

high latitudes. Difficulties of modeling the high latitude ionospheric ion composition using IS spectra include the presence of plasma instabilities, which distort IS spectra [Akbari et al., 2012], non-Maxwellian IS spectra for aspect angles (the angle between the local geomagnetic field and the ISR beam) > 30^o [Raman et al., 1981, Hubert and Lathuillere, 1989], and the dynamic nature of ion compositions caused in part by electric field disturbances and frictional heating [Zettergren et al., 2010, and references therein]. Although there have been successful techniques to model the ion composition, they are of limited use in the high latitude ionosphere. Cabrit and Kofman [1997], Shibata et al. [2000]'s techniques are successful when the ionosphere is undisturbed by strong electric fields and frictional heating, while Blelly et al. [1996], Jenkins et al. [1997]'s techniques are good for periods of extended heating. However, for dynamic heating events (< 1 min) such as an auroral event, the plasma time history must be known because the plasma can remain disturbed for extended time periods while also convecting to other three dimensional locations [Zettergren et al., 2010, 2014]. Zettergren et al. [2010, 2011], Zettergren [2009] have modeled the high latitude ion composition using ISR data with the assumption that the effective electric field remains constant for dynamic heating events. However, as they noted, the effective electric field does not necessarily remain constant with altitude, especially due to altitude dependent neutral winds.

An important part of the ionosphere-magnetosphere system is ion outflow: ions escaping the ionosphere into the magnetosphere. One known cause of ion outflow are dynamic auroral events [Moore and Horwitz, 2007]. Questions concerning ion outflow include what ions are leaving and how many are leaving. ISR data is useful and plentiful in answering this question, but only if the correct ion composition is known. Thus, a technique to determine the correct ion composition for short integration time ISR scans is needed.

This thesis expands upon the work done of Zettergren et al. [2011, 2010] and Zettergren [2009] by incorporating two new models that account for neutral winds, altitude based variations in magnetic and effective electric fields, and more sophisticated treatment of collisions. Zettergren et al. [2011] systematically and self consistently accounted for dynamic ion composition variations, however, the crossover

altitude, z_c, which represents the transition between a molecular domination plasma to an atomic plasma, may be higher than what theory predicts and neutral winds are not accounted for separately, which we show is significant.

1.2 Outline of Thesis

Chapter 2 reviews the methodology of Zettergren et al. [2011] and then proceeds to detail the new models developed for this work. This section includes overviews of Horizontal Wind Model 2007 (HWM), International Geomagnetic Reference Field (IGRF), and the anisotropic models for ion temperatures and how they are used in this work.

Chapter 3 details results of the models applied to Sondrestrom ISR datasets. Specifically, this looks at different model outputs for temperature profiles and how they differ from each other.

Chapter 4 details the results of the models applied to Sonderstrom ISR datasets. This includes statistical analysis, including storm only, quiet only ($K_p < 3$), and K_p specific results.

Chapter 5 summarizes the results of the thesis, lists perceived contributions, and outlines the limitations of the work done along with some ideas of how to address those limitations.

Chapter 2

Methodology

The approach taken in this work is to self-consistently model line-of-sight ion temperatures using three different models referred to as A, B, and C. Model A is the reference model for the work done by Zettergren et al. [2011] but includes an altitude dependent magnetic field. This model estimates the effective electric field which implicitly includes neutral wind effects. Model B expands upon Model A by including neutral winds calculated via the HWM. Model C incorporates Coulomb collisions into calculations of the 13-moment momentum, energy, and pressure tensor equations.

2.1 Model Fitting

Models A, B, and C approximate the overall ion temperature based on altitude and a set of parameters $\boldsymbol{x}$. We further distinguish between model quantities, $\boldsymbol{x}_{data}$, which are used as inputs into the temperature model, and estimated quantities, $\boldsymbol{x}_{est}$, which the temperature models estimate to determine the ion composition. The model quantities are: the horizontal winds, u_x and u_y, from HWM (Models B and C only); the geomagnetic field calculated using the IGRF, B_x, B_y, and B_z; the radar beam angle, ϕ; the MSIS thermospheric model derived parameters of neutral temperature, T_n, atomic oxygen density, n_O, molecular oxygen density, n_{O_2}, and molecular nitrogen density, n_{N_2}; and the radar derived electron density and

electron temperature inte rpolated onto the altitude profile, n_e and T_e, respectively (Models B and C only). The estimated quantities vary depending on the model used. Model A estimates the effective perpendicular electric field, $\boldsymbol{E}'_{\perp}$, and the crossover altitude, z_c, which is a function of the ion composition, p, as defined in Equation (2.1), according to Oliver [1975] as shown in Equation (2.2). Models B and C estimate the perpendicular electric field components, E_x and E_y, the crossover altitude, z_c, and the scale height, H.

$$p \equiv \frac{n_{\mathrm{O}^+}}{n_{\mathrm{e}^-}} \tag{2.1}$$

$$p(z, \boldsymbol{x}_{est}) = \frac{2}{1 + \sqrt{1 + 8\exp(-\frac{z - z_c}{H})}} \tag{2.2}$$

The crossover altitude, z_c, is where $p = 0.5$ (50% O^+ and 50% molecular ions) and H is a scale height parameter which determines the composition altitude variation spread. As is seen from Equation (2.2) and Figure 2.1 on page 11, p can vary greatly depending on the estimated quantities of z_c and H, which are assumed to be related to the parameters in $\boldsymbol{x}_{data}$, and possibly other parameters, in an unknown manner.

The estimated parameters are determined by fitting the model temperature, T_{model}, to the radar temperature, T_{radar} (which has been linearly interpolated onto an altitude profile), in a least squares sense. However, T_{model} and T_{radar} use different ion compositions and need to be related to each other. This relation is given by Zettergren et al. [2011] and Zettergren [2009] in the following relation:

$$T_{model} = \frac{F_i(p_{model})}{F_i(p_{radar})} T_{radar} \tag{2.3}$$

which is derived from work done by Waldteufel [1971], where the F_i relation is given by [Waldteufel, 1971]:

$$F_i(p) = -2.902 + 0.785p + \frac{8.2}{p + 2.1} \tag{2.4}$$

and similarly for electron temperatures [Waldteufel, 1971]:

$$F_e(p) = 1.017 - 0.524p + 0.189(p - 0.45)^3 \tag{2.5}$$

$\boldsymbol{x}_{est}$ is found by solving the least squares problem:

$$\boldsymbol{x}_{est} = \arg\min_{\boldsymbol{x}} \left\{ \sum_k \left[T_{model}(z_k; \boldsymbol{x}_k) - \frac{F_i(p_{model_k})}{F_i(p_{radar_k})} T_{radar_k}(z_k) \right]^2 \right\} \tag{2.6}$$

In Equation (2.6), k is indexing the altitudes of profile measurements over which the minimization procedure occurs, typically 100-500 km. That is, k indexes every data point location for the fit.

The ion temperature is a density-weighted combination of O^+ and NO^+ temperatures as approximately given by Jenkins et al. [1997]:

$$T_i = p(T_{O^+} - T_{NO^+}) + T_{NO^+} \tag{2.7}$$

It is noted in Zettergren et al. [2011] that the approximation of ion temperature in the ionosphere being a weighted sum of the constituent species is a reasonable approximation in a plasma dominated by O^+ and NO^+. In Equation (2.7), the calculation of the species' temperatures vary depending on the model. However, in all three models, each specie's temperature is a combination of the parallel and perpendicular temperatures given by [Raman et al., 1981]:

$$T_s = T_{s\parallel} \cos^2 \phi + T_{s\perp} \sin^2 \phi \tag{2.8}$$

where s is the ion species, either O^+ or NO^+, and ϕ, the aspect angle, is the angle between the local geomagnetic field and the radar beam [Hubert and Lathuillere, 1989, Gaimard et al., 1996]. The analysis done in this paper does not recompute the ISR data from the IS spectrum. For ϕ greater than 30^o with respect to the geomagnetic field, the ISR data must be recomputed taking into effect the IS spectrum changes caused by non-Maxwellian effects.

2.2 Model A

For Model A, the parallel [St.-Maurice et al., 1999] and perpendicular [Winkler et al., 1992] ion temperatures are given by the semi-empirical equation:

$$T_{sq} = T_n + \frac{1}{2}\beta_{sq}\frac{<m_n>}{k_b}\frac{1}{1+(\nu_s/\Omega_s)^2}\frac{E_\perp'^2}{B^2} \tag{2.9}$$

Here, (2.9), q is either $\parallel$ or $\perp$, T_n is the neutral temperature, β_{sq} is a collision-type-dependent coefficient which describes temperature anisotropies [Winkler et al., 1992, McCrea et al., 1993], $<m_n>$ is the average mass of the neutral atmospheric constituents, k_b is the Boltzmann constant, ν_s is the ion-neutral collision frequency, Ω_s is the ion gyrofrequency, and B is the geomagnetic field strength. The parallel and perpendicular versions of Equation (2.9) can be combined with Equation (2.8) as shown in Zettergren et al. [2011] to get the ISR line-of-sight ion specific temperature:

$$T_s = T_n + \left(\beta_{s\parallel}\cos^2\phi + \beta_{s\perp}\sin^2\phi\right)\left[\frac{1}{2}\frac{<m_n>}{k_b}\frac{1}{1+(\nu_s/\Omega_s)^2}\frac{1}{B^2}\right]E_\perp'^2 \tag{2.10}$$

All values are known in Equation (2.10) except $\boldsymbol{E}'_\perp$, the electric field in the neutral frame of reference, for which $\boldsymbol{E}'_\perp = \boldsymbol{E}_\perp + \boldsymbol{u}_{\perp n}\times\boldsymbol{B}$. In Model A, $\boldsymbol{E}_\perp$ and $\boldsymbol{u}_{\perp n}$ are implicitly estimated when $\boldsymbol{E}'_\perp$ is estimated. $|\boldsymbol{E}'_\perp|$ is estimated for when the composition is supposedly known, the E region (<150 km). All ions are assumed here to be molecular, which is used to set T_s at a correct value. Then, $\boldsymbol{E}'_\perp$ is chosen such that $T_{model} = T_{radar}$ in this limited region. As noted in Zettergren et al. [2011], temperature measurements from the 130-150 km region are used to estimate $\boldsymbol{E}'_\perp$ using a weighted least squares approach.

The above method of estimating $\boldsymbol{E}'_\perp$ requires the assumption that $\boldsymbol{E}'_\perp$ does not change with altitude. However, this is not necessarily the case and $\boldsymbol{u}_{\perp n}$ does vary with altitude, even though $\boldsymbol{E}_\perp$ won't, as seen below in Figures 2.2 and 2.3 located on page 13 under section 2.3. It is noted that Model A estimates $\boldsymbol{x}_{est}$ sequentially;

Model A estimates $\boldsymbol{E}'_{\perp}$ and then uses that estimate to estimate z_c.

Magnetic Field Calculation

The Earth's magnetic field varies with latitude, longitude, altitude, time, and various external factors. The International Geomagnetic Reference Field (IGRF) model is used to calculate the magnetic field for varying latitudes, longitudes, altitudes, and times. This model represents the geomagnetic field produced by Earth's internal sources according to $\boldsymbol{B} = -\nabla V$ where V is given in Equation (2.11) below.

$$V(r,\theta,\phi,t) = a\sum_{n=1}^{N}\sum_{m=0}^{n}\left(\frac{a}{r}\right)^{n+1}\left[g_n^m(t)\cos m\phi + h_n^m(t)\sin m\phi\right]P_n^m(\cos\theta) \qquad (2.11)$$

In Equation (2.11), the numerical Gauss coefficients (Schmidt semi-normalized spherical harmonic coefficients) h_n^m and g_n^m, which were calculated with data from multiple satellites and observatories around the world, are valid for the years 1900.0 - 2015.0 and definitive for the years 1945.0 - 2005.0 [Finlay et al., 2010]. The ISR datasets used span from 1998 through 2008. $P_n^m(\cos\theta)$ are the Schmidt semi-normalized associated Legendre functions of degree n and order m. r represents the radial distance from the center of the Earth and a is 6372.1 km (the magnetic reference spherical radius).

2.3 Model B

Model B differs from Model A in three important ways: it finds $\boldsymbol{x}_{est}$ simultaneously whereas Model A estimates $\boldsymbol{E}'_{\perp}$ and then estimates z_c; it explicitly includes the effects of the neutral wind via the HWM, thus estimating E_x and E_y; and, it allows for variation of H.

Model B uses the same equations as Model A but there are more unknowns since E_x and E_y are estimated at every altitude point instead of estimating $\boldsymbol{E}'_{\perp}$ for the entire temperature profile. Due to the amount of unknowns, only field aligned

beams are used for the radar so that $\boldsymbol{E}_\perp$ (E_x and E_y) may be considered constant due to large parallel conductivities in the ionosphere. This reduces the unknowns from 2k+2, z_c, H, and E_x and E_y at every altitude location k, to 4, z_c, H, E_x, and E_y. In this study, field aligned beams are beams within 10^o of the magnetic field: $170^o - 190^o$. The 10^o alters the line of sight temperature according to Equation (2.8). Thus, the perpendicular temperature is included by a factor of only 0.03, a negligible amount. This also assumes that the electric fields will remain constant over this small deviation.

In a nonlinear least squares fit, initial guesses for $\boldsymbol{x}_{est}$ must be made. The initial guess for the electric field is made by calculating $|\boldsymbol{E}'_\perp|$ and then assuming equal components:

$$E_x = E_y = \frac{E'_\perp}{\sqrt{2}} \tag{2.12}$$

These values are constrained by the fitter to be $\pm$ 250mV/m. The crossover altitude is constrained such that unphysically low altitude high concentrations of NO^+ do not occur: $140 \leq z_c \leq 500$ km. As there is no definitive view on what z_c and H values should be, the constraining of these values took several trial runs until qualitatively physical results appeared. Thus, it was found that bounding H between 10 and 50 km seems the most reasonable. A more in-depth look at the relationship of z_c, H, and p is presented below.

Ion Parameterization

Oliver [1975]'s equation for ion composition, Equation (2.2), has explicit dependencies on the crossover altitude and, as it will be shown in Section 4, an implicit dependency on $\boldsymbol{E}'_\perp$. In order to get an intuitive feel for H and Z_c, refer to Figure 2.1 below. It is shown that H greater than 50 often leads to high concentrations of O^+ below 100 km. In this study, H is bound between 10 and 50 km (the red, blue, and green profiles).

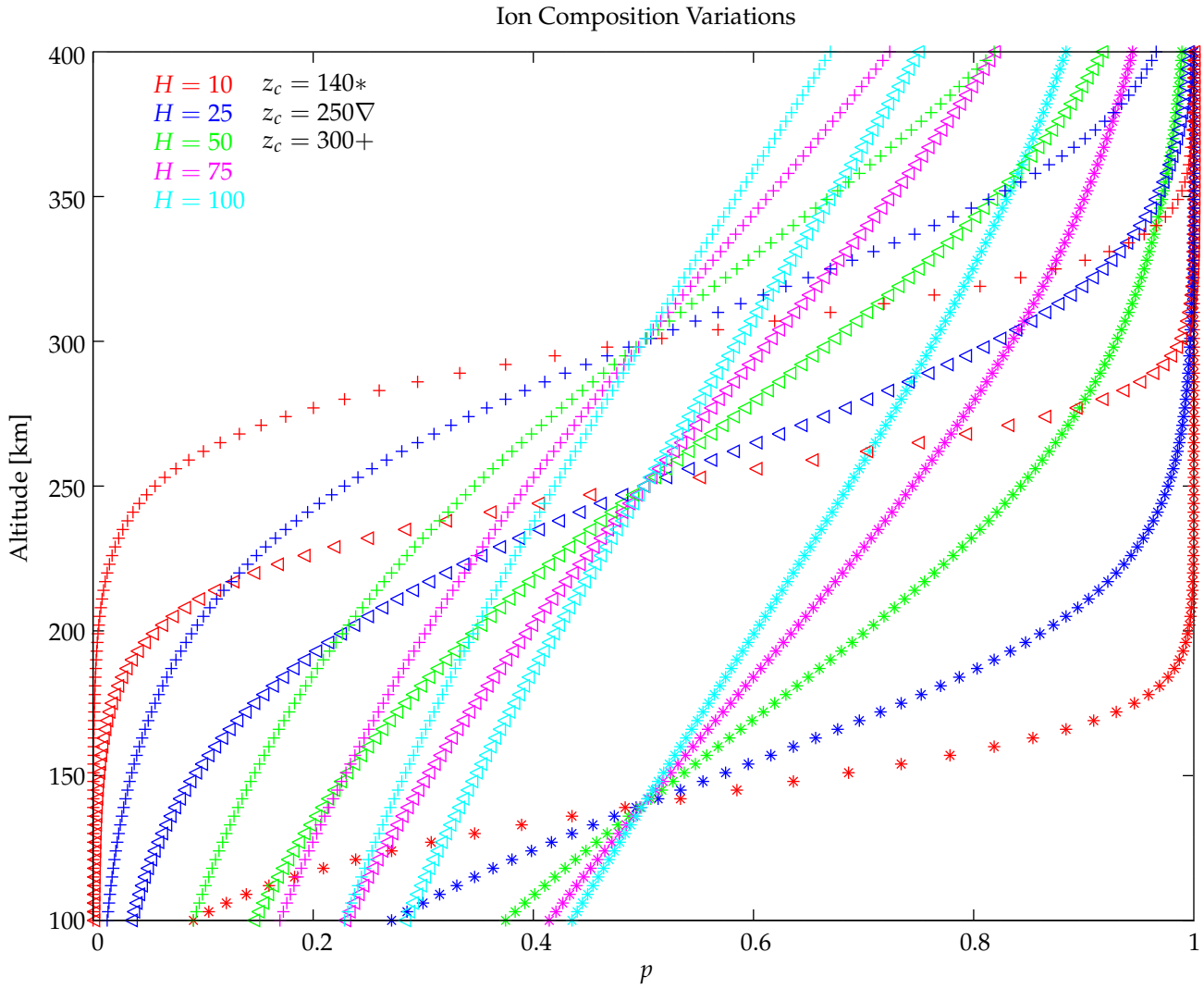

Figure 2.1: The effects of scale height and crossover altitude on ion parameterization.

Wind Field Calculation

The horizontal wind model 2007 (HWM), an empirical model, is used to calculate the winds at the various beam locations and times. HWM contains no solar activity dependence, making the nighttime wind field values questionable [Drob

et al., 2008]. The model calculates both quiet time winds and disturbance winds and combines them linearly to get the total wind field. The disturbance winds only depend on magnetic latitude, magnetic local time, and K_p, while height, seasonal, and solar activity dependencies are not yet included; they represent average disturbance winds above 225 km [Drob et al., 2008]. However, this model still fits the empirical data better than previous wind models [Drob et al., 2008]. Ideally, there would be a Fabry-Pérot wind measurement dataset to go with each ISR dataset. However, this is not always the case, thus HWM is used as a best, default option. In this study, no FPI wind data is included.

Figures 2.2 and 2.3 are representative of possible wind fields at Sondrestrom for midnight and noon UT, respectively. Wind speeds greater than 250 $^{\mathrm{m}}/_{\mathrm{s}}$ are possible which is significant since wind speeds of 200 $^{\mathrm{m}}/_{\mathrm{s}}$ add about 5 $^{\mathrm{mV}}/_{\mathrm{m}}$ to $\boldsymbol{E}'_{\perp}$ through $\boldsymbol{u} \times \boldsymbol{B}$. Wind shears are common below 400 km, both in terms of wind speeds, and the direction of flow. Also of note is that in Figure 2.2, the meridonial wind is negative for all altitudes whereas the zonal component is positive for all values above 130 km. This is contrasted with Figure 2.3 which has the meridonial wind roughly equal to zero up until 225 km where it then becomes positive, and the zonal wind which is negative above 120 km. Thus, wind fields can vary greatly throughout the day and wind shears are common up until 400 km.

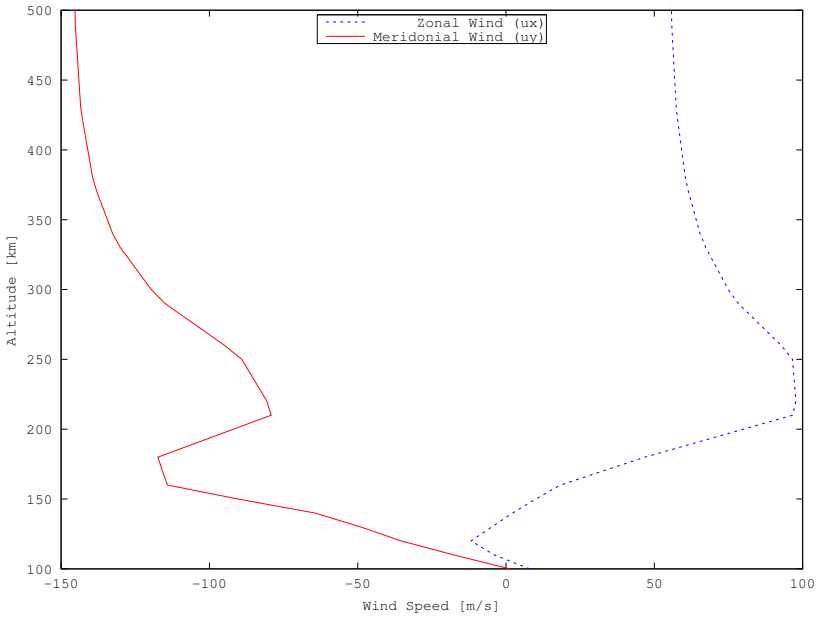

Figure 2.2: Wind field given by HWM for 12 November 2003 midnight UT at Sondrestrom.

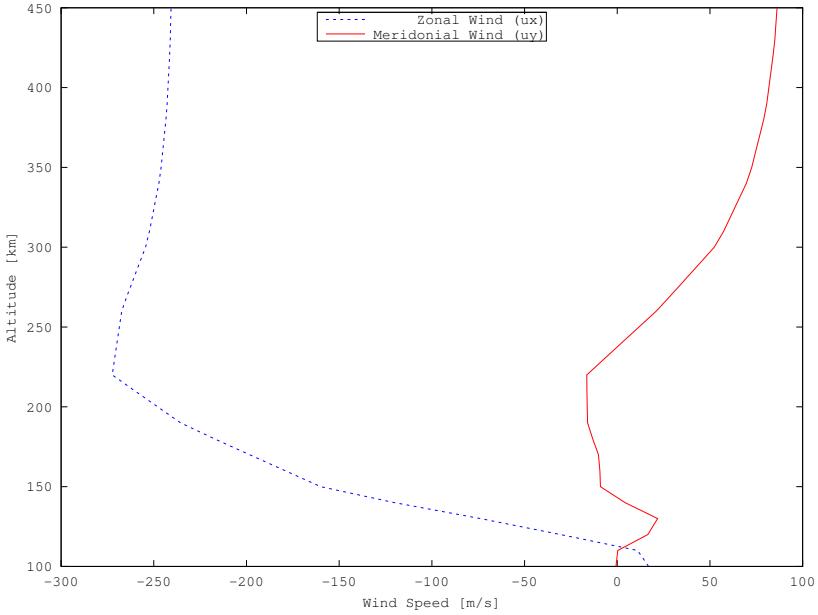

Figure 2.3: Wind field given by HWM for 28 August 1998 noon UT at Sondrestrom.

2.4 Model C

Model C calculates the ion specific temperatures, T_{O^+} and T_{NO^+}, differently than in Models A and B. The strength of Model C is that it incorporates ion-ion collisions. These equations are outlined below and are the direct solution of the 13-moment equations rather than semi-empirical results. The main assumption is that the plasma from 100-500 km is a steady-state, collision dominated, plasma.

Collision Frequencies

The collision frequencies are calculated as shown in Schunk and Nagy [2000]. In the high latitude ionosphere the species of concern are the ions O^+ and NO^+, the neutrals O, N_2 and O_2, and the electron, e^-. For ion neutral collision frequencies, Equation (2.13) is used:

$$\nu_{sn} = C_{sn} n_n \tag{2.13}$$

In Equation (2.13), C_{sn} is given in Schunk and Nagy [2000, page 97] for nonresonant interactions and Schunk and Nagy [2000, page 99] for the resonant interaction, O^+ with O, and n_n is the neutral's number density in cm^{-3}. The ion-ion collision frequency is given below as [Schunk and Nagy, 2000]:

$$\nu_{sj} = B_{sj} \frac{n_j}{T_j^{3/2}} \tag{2.14}$$

In Equation (2.14), s and j are either O^+ or NO^+, B_{sj} is a numerical coefficient given in Schunk and Nagy [2000, page 96], n_j is the number density in cm^{-3}, and T_j is the temperature in Kelvins. The ion-electron collision frequency is given below in Equation (2.17) which is derived from Equations (2.15)[Schunk and Nagy, 2000] and (2.16).

$$\nu_{e^- s} = 54.5 \frac{n_s Z_s^2}{T_{e^-}^{3/2}} \tag{2.15}$$

$$n_s m_s \nu_{se^-} = n_{e^-} m_{e^-} \nu_{e^- s} \tag{2.16}$$

$$\nu_{se^-} = 54.5 \frac{n_{e^-} m_{e^-}}{m_s} \frac{Z_s^2}{T_{e^-}^{3/2}} \tag{2.17}$$

In Equations (2.15), (2.16), and (2.17) above, e^- represents an electron, and Z_s is the s species' particle charge number (1 for present studies). Equation (2.16) represents conservation of momentum between collisions of ions and electrons.

Ion Drift: Momentum Equation

The perpendicular ion drift velocities are given below in Equation (2.19) and depend on $E'_\perp$, the ion-neutral collision rate, and gyro-frequency. The drift equation is derived from the Schunk [1977] 13-moment approximation which is valid for both large temperature and large drift velocity differences. This equation is given below in Equation (2.18) along with the assumption that the equation is dominated by electromagnetic forces.

$$\frac{\delta M_s}{\delta t} = -\sum_n n_s m_s \nu_{sn} (\boldsymbol{u}_s - \boldsymbol{u}_n) = q\boldsymbol{E}_\perp + q(\boldsymbol{u}_s) \times \boldsymbol{B} \tag{2.18}$$

$$u_{\perp s} = \sqrt{\frac{1}{1+\alpha_s^2} \left(\frac{\boldsymbol{E}_\perp + \boldsymbol{u}_{\perp n} \times \boldsymbol{B}}{B} \right)^2} \tag{2.19}$$

In Equation (2.19) above, u_s is the ion drift speed and α_s is given below in Equation (2.20).

$$\alpha_s = \frac{\sum \nu_{sn}}{\Omega_s} \tag{2.20}$$

Energy

From the energy balance below in (2.23) [Schunk, 1977, equations 41 (ion-ion) and 50 (ion-neutral)] the average ion temperatures, T_{O^+} and T_{NO^+}, are derived for input into the pressure tensor relations given later.

For ion-ion collisions we assume the species temperature differences are small in comparison to the average gas temperature and the species drift velocities are small compared to the species thermal speeds.

$$\left[\frac{\delta E_s}{\delta t}\right]_{ion-ion} = -\sum_j \frac{n_s m_s \nu_{sj}}{m_s + m_j} 3k_b(T_s - T_j) \tag{2.21}$$

For ion-neutral collisions, the following equation is valid for both large temperature and large drift velocity differences.

$$\left[\frac{\delta E_s}{\delta t}\right]_{ion-neutral} = -\sum_s \frac{n_s m_s \nu_{sn}}{m_s + m_n} \left[3k_b(T_s - T_n) - m_n(\boldsymbol{u}_s - \boldsymbol{u}_n)^2\right] \tag{2.22}$$

Combination of Equations (2.21) and (2.22) leads to Equation (2.23) below.

$$\left[\frac{\delta E_s}{\delta t}\right]_{total} = -\sum_j \frac{n_s m_s \nu_{sj}}{m_s + m_j} 3k_b(T_s - T_j) - \sum_s \frac{n_s m_s \nu_{sn}}{m_s + m_n} \left[3k_b(T_s - T_n) - m_n(\boldsymbol{u}_s - \boldsymbol{u}_n)^2\right] = 0 \tag{2.23}$$

Two such equations are solved for $s = \mathrm{O}^+$ and $s = \mathrm{NO}^+$ yielding:

$$T_{\mathrm{O}^+} = C_{1\mathrm{O}^+} T_n + C_{2\mathrm{O}^+} T_e + \frac{(C_{3\mathrm{O}^+}) u^2_{\perp \mathrm{O}^+}}{3k_b} \tag{2.24a}$$

$$T_{\mathrm{NO}^+} = C_{1\mathrm{NO}^+} T_n + C_{2\mathrm{NO}^+} T_e + \frac{(C_{3\mathrm{NO}^+}) u^2_{\perp \mathrm{NO}^+}}{3k_b} \tag{2.24b}$$

In Equation (2.24) above, the C terms are coefficients determined by collision frequencies and mass, defined below.

$$C_{1O^+} = \frac{a_{O^+} + b_{O^+NO^+} a_{NO^+}}{1 - b_{O^+NO^+} b_{NO^+O^+}} \tag{2.25a}$$

$$C_{2O^+} = \frac{c_{O^+e^-} + b_{O^+NO^+} c_{NO^+e^-}}{1 - b_{O^+NO^+} b_{NO^+O^+}} \tag{2.25b}$$

$$C_{3O^+} = \frac{d_{O^+} + b_{O^+NO^+} d_{NO^+}}{1 - b_{O^+NO^+} b_{NO^+O^+}} \tag{2.25c}$$

$$C_{1NO^+} = \frac{a_{NO^+} + b_{NO^+O^+} a_{O^+}}{1 - b_{O^+NO^+} b_{NO^+O^+}} \tag{2.25d}$$

$$C_{2NO^+} = \frac{c_{NO^+e^-} + b_{NO^+O^+} c_{O^+e^-}}{1 - b_{O^+NO^+} b_{NO^+O^+}} \tag{2.25e}$$

$$C_{3NO^+} = \frac{d_{NO^+} + b_{NO^+O^+} d_{O^+}}{1 - b_{O^+NO^+} b_{NO^+O^+}} \tag{2.25f}$$

The unknowns a, b, c, and d in Equation (2.25) are defined below.

$$a_{O^+} = \frac{\overline{\nu_{O^+n}}}{\nu_{O^+}} \tag{2.26a}$$

$$a_{NO^+} = \frac{\overline{\nu_{NO^+n}}}{\nu_{NO^+}} \tag{2.26b}$$

$$b_{O^+NO^+} = \frac{\frac{\nu_{O^+NO^+}}{m_{O^+} + m_{NO^+}}}{\nu_{O^+}} \tag{2.26c}$$

$$b_{NO^+O^+} = \frac{\frac{\nu_{NO^+O^+}}{m_{NO^+} + m_{O^+}}}{\nu_{NO^+}} \tag{2.26d}$$

$$c_{O^+e^-} = \frac{\frac{\nu_{O^+e^-}}{m_{O^+} + m_{e^-}}}{\nu_{O^+}} \tag{2.26e}$$

$$c_{NO^+e^-} = \frac{\frac{\nu_{NO^+e^-}}{m_{NO^+} + m_{e^-}}}{\nu_{NO^+}} \tag{2.26f}$$

$$d_{O^+} = \frac{\sum_n \frac{m_n \nu_{O^+n}}{m_{O^+} + m_n}}{\nu_{O^+}} \tag{2.26g}$$

$$d_{NO^+} = \frac{\sum_n \frac{m_n \nu_{NO^+n}}{m_{NO^+} + m_n}}{\nu_{NO^+}} \tag{2.26h}$$

In Equation (2.26) above, $\overline{\nu_{O^+}}$ and $\overline{\nu_{NO^+}}$ represents the mass weighted sum of the species' neutral collisions as shown in Equation (2.27) below, and ν_{O^+} and ν_{NO^+} represent the sum of mass weighted collision frequencies for those species as shown in Equation (2.28) below.

$$\overline{\nu_{O^+n}} = \sum_n \frac{\nu_{O^+n}}{m_{O^+} + m_n} \tag{2.27a}$$

$$\overline{\nu_{NO^+n}} = \sum_n \frac{\nu_{NO^+n}}{m_{NO^+} + m_n} \tag{2.27b}$$

$$\nu_{O^+} = \overline{\nu_{O^+n}} + \frac{\nu_{O^+NO^+}}{m_{O^+} + m_{NO^+}} + \frac{\nu_{O^+e^-}}{m_{O^+} + m_{e^-}} \tag{2.28a}$$

$$\nu_{NO^+} = \overline{\nu_{NO^+n}} + \frac{\nu_{NO^+O^+}}{m_{NO^+} + m_{O^+}} + \frac{\nu_{NO^+e^-}}{m_{NO^+} + m_{e^-}} \tag{2.28b}$$

Pressure Tensor

The 13-moment pressure tensor equation, along with all of the previous equations, is used to calculate the $\parallel$ and $\perp$ temperatures for O^+ and NO^+. The O^+ temperatures are given in Equation (2.35) below and the NO^+ temperatures are given in Equation (2.36) below. These are derived from Schunk [1977, equations 41 (ion-ion) and 50 (ion-neutral)] for ion-ion, Equation (2.29), and ion-neutral, Equation (2.30), interactions, which, when combined, result in Equation (2.31).

$$\left[\frac{\delta \overleftrightarrow{P}_s}{\delta t}\right]_{ion-ion} = -\sum_{j \neq s} \frac{2 m_s \nu_{sj}}{m_s + m_j} \left\{ \overleftrightarrow{P}_s - \frac{n_s}{n_j} \overleftrightarrow{P}_j + \frac{3}{10} z''_{sj} \frac{m_j}{m_s} \left[\overleftrightarrow{\tau}_s + \frac{\rho_s}{\rho_j} \overleftrightarrow{\tau}_j \right] \right\} - \frac{3}{5} z''_{ss} \nu_{ss} \overleftrightarrow{\tau}_s \tag{2.29}$$

$$\left[\frac{\delta \overleftrightarrow{P}_s}{\delta t}\right]_{ion-neutral} = -\sum_n \frac{2m_s\nu_{sn}}{m_s+m_n}\left\{\overleftrightarrow{P}_s - \frac{n_s}{n_n}\overleftrightarrow{P}_n - n_s m_n(\boldsymbol{u}_s-\boldsymbol{u}_n)(\boldsymbol{u}_s-\boldsymbol{u}_n)+ \frac{3}{4}\frac{m_n}{m_s}Q_{\mathrm{O^+n}}\left[\overleftrightarrow{\tau}_s + \frac{\rho_s}{\rho_n}\overleftrightarrow{\tau}_n + \rho_s(\boldsymbol{u}_s-\boldsymbol{u}_n)(\boldsymbol{u}_s-\boldsymbol{u}_n)- \frac{\rho_s}{3}(\boldsymbol{u}_s-\boldsymbol{u}_n)^2\right]\right\} \tag{2.30}$$

$$\left[\frac{\delta \overleftrightarrow{P}_s}{\delta t}\right]_{total} = \left[\frac{\delta \overleftrightarrow{P}_s}{\delta t}\right]_{ion-ion} + \left[\frac{\delta \overleftrightarrow{P}_s}{\delta t}\right]_{ion-neutral} \tag{2.31}$$

In Equation (2.30) above, $Q_{\mathrm{O^+n}}$ is a ratio of scattering cross sections as defined in Gaimard, St-Maurice, Lathuillere, and Hubert [1998] with $Q_{\mathrm{O^+}n} \equiv \frac{Q_{sn}^{(2)}}{Q_{sn}^{(1)}}$. In Equations (2.29) and (2.30) above, $\overleftrightarrow{P}_s$, $\overleftrightarrow{\tau}_s$, and $\overleftrightarrow{\tau}_n$ are defined in Equations (2.32), (2.33), and (2.34) below, respectively.

$$\overleftrightarrow{P}_s = \begin{array}{c} \\ \hat{e_x} \\ \hat{e_y} \\ \hat{e_z} \end{array} \begin{array}{c} \begin{array}{ccc} \hat{e_x} & \hat{e_y} & \hat{e_z} \end{array} \\ \begin{pmatrix} n_s k_b T_{s\perp} & 0 & 0 \\ 0 & n_s k_b T_{s\perp} & 0 \\ 0 & 0 & n_s k_b T_{s\parallel} \end{pmatrix} \end{array} \tag{2.32}$$

$$\overleftrightarrow{\tau}_s = \overleftrightarrow{P}_s - n_s k_b T_s \overleftrightarrow{I} \tag{2.33}$$

$$\overleftrightarrow{\tau}_n = 0 \qquad \text{(since neutrals are isotropic)} \tag{2.34}$$

In Equation (2.33) above, $\overleftrightarrow{I}$ is the 3x3 identity matrix. The following is noted for the below temperature equations: $T_{s\parallel}$ is found via the $\hat{e_z}\hat{e_z}$ pressure tensor equation component and $T_{s\perp}$ is found via adding the $\hat{e_x}\hat{e_x}$ and $\hat{e_y}\hat{e_y}$ pressure tensor equation components.

$$T_{O^+\parallel} = K_{1O^+} T_{O^+} + K_{2O^+} T_n + K_{3O^+{}_\parallel} u^2_{\perp O^+} + K_{4O^+} T_{NO^+} + K_{5O^+} T_{e^-} \tag{2.35a}$$

$$T_{O^+\perp} = K_{1O^+} T_{O^+} + K_{2O^+} T_n + K_{3O^+{}_\perp} u^2_{\perp O^+} + K_{4O^+} T_{NO^+} + K_{5O^+} T_{e^-} \tag{2.35b}$$

$$T_{NO^+\parallel} = K_{1NO^+} T_{NO^+} + K_{2NO^+} T_n + K_{3NO^+{}_\parallel} u^2_{\perp NO^+} + K_{4NO^+} T_{O^+} + K_{5NO^+} T_{e^-} \tag{2.36a}$$

$$T_{NO^+\perp} = K_{1NO^+} T_{NO^+} + K_{2NO^+} T_n + K_{3NO^+{}_\perp} u^2_{\perp NO^+} + K_{4NO^+} T_{O^+} + K_{5NO^+} T_{e^-} \tag{2.36b}$$

In Equations (2.35) and (2.36) above, the unknown K terms are defined below in Equations (2.37) and (2.38), respectively.

$$K_{1O^+} = \frac{e_{O^+} + o_{O^+NO^+} h_{NO^+O^+}}{\Delta_K} \tag{2.37a}$$

$$K_{2O^+} = \frac{f_{O^+} + o_{O^+NO^+} f_{NO^+}}{\Delta_K} \tag{2.37b}$$

$$K_{3O^+{}_\parallel} = \frac{g_{O^+\parallel} + o_{O^+NO^+} g_{NO^+\parallel}}{\Delta_K} \tag{2.37c}$$

$$K_{3O^+{}_\perp} = \frac{g_{O^+\perp} + o_{O^+NO^+} g_{NO^+\perp}}{\Delta_K} \tag{2.37d}$$

$$K_{4O^+} = \frac{h_{O^+NO^+} + o_{O^+NO^+} e_{NO^+}}{\Delta_K} \tag{2.37e}$$

$$K_{5O^+} = \frac{k_{O^+e^-} + o_{O^+NO^+} k_{NO^+e^-}}{\Delta_K} \tag{2.37f}$$

$$K_{1NO^+} = \frac{e_{NO^+} + o_{NO^+O^+} h_{O^+NO^+}}{\Delta_K} \tag{2.38a}$$

$$K_{2NO^+} = \frac{f_{NO^+} + o_{NO^+O^+} f_{O^+}}{\Delta_K} \tag{2.38b}$$

$$K_{3NO^+{}_{\parallel}} = \frac{g_{NO^+\parallel} + o_{NO^+O^+} g_{O^+\parallel}}{\Delta_K} \tag{2.38c}$$

$$K_{3NO^+{}_{\perp}} = \frac{g_{NO^+\perp} + o_{NO^+O^+} g_{O^+\perp}}{\Delta_K} \tag{2.38d}$$

$$K_{4NO^+} = \frac{h_{NO^+O^+} + o_{NO^+O^+} e_{O^+}}{\Delta_K} \tag{2.38e}$$

$$K_{5NO^+} = \frac{k_{NO^+e^-} + o_{NO^+O^+} k_{O^+e^-}}{\Delta_K} \tag{2.38f}$$

In Equations (2.37) and (2.38) above, the unknown coefficients are given below in Equations (2.39) and (2.40), respectively, along with Δ_K in Equation (2.41).

$$e_{O^+} = \left[\sum_n \left(\frac{2m_{O^+}\nu_{O^+n}}{m_{O^+}+m_n}\frac{3}{4}\frac{m_n}{m_{O^+}}Q_{O^+n}\right) + \frac{6}{5}\nu_{O^+NO^+}\frac{m_{NO^+}}{m_{O^+}+m_{NO+}} + \frac{6}{5}\nu_{O^+e^-}\frac{m_{e^-}}{m_{O^+}+m_{e^-}} + \frac{6}{5}\nu_{O^+O^+}\right](\zeta_{O^+})^{-1} \tag{2.39a}$$

$$f_{O^+} = \frac{\sum_n \frac{2m_{O^+}\nu_{O^+n}}{m_{O^+}+m_n}}{\zeta_{O^+}} \tag{2.39b}$$

$$g_{O^+\perp} = \frac{\sum_n \frac{2m_{O^+}\nu_{O^+n}}{m_{O^+}+m_n}\left(\frac{1}{2}\frac{m_n}{k_b} - \frac{1}{6}\frac{m_n}{k_b}Q_{O^+n}\right)}{\zeta_{O^+}} \tag{2.39c}$$

$$g_{O^+\parallel} = \frac{\sum_n \frac{2m_{O^+}\nu_{O^+n}}{m_{O^+}+m_n}\frac{1}{4}\frac{m_n}{k_b}Q_{O^+n}}{\zeta_{O^+}} \tag{2.39d}$$

$$h_{O^+NO^+} = \frac{\frac{6}{5}\frac{m_{O^+}\nu_{O^+NO^+}}{m_{O^+}+m_{NO^+}}}{\zeta_{O^+}} \tag{2.39e}$$

$$k_{O^+e^-} = \frac{2\frac{m_{O^+}\nu_{O^+e^-}}{m_{O^+}+m_{e^-}}}{\zeta_{O^+}} \tag{2.39f}$$

$$o_{O^+NO^+} = \frac{\frac{4}{5}\frac{m_{O^+}\nu_{O^+NO^+}}{m_{O^+}+m_{NO^+}}}{\zeta_{O^+}} \tag{2.39g}$$

$$e_{\mathrm{NO^+}} = \left[\sum_n \left(\frac{2m_{\mathrm{NO^+}}\nu_{\mathrm{O^+}n}}{m_{\mathrm{NO^+}}+m_n}\frac{3}{4}\frac{m_n}{m_{\mathrm{NO^+}}}Q_{\mathrm{NO^+}n}\right) + \frac{6}{5}\nu_{\mathrm{NO^+O^+}}\frac{m_{\mathrm{O^+}}}{m_{\mathrm{NO^+}}+m_{\mathrm{O+}}} + \frac{6}{5}\nu_{\mathrm{NO^+e^-}}\frac{m_{\mathrm{e^-}}}{m_{\mathrm{NO^+}}+m_{\mathrm{e^-}}} + \frac{6}{5}\nu_{\mathrm{NO^+NO^+}}\right](\zeta_{\mathrm{NO^+}})^{-1} \tag{2.40a}$$

$$f_{\mathrm{NO^+}} = \frac{\sum_n \frac{2m_{\mathrm{NO^+}}\nu_{\mathrm{NO^+}n}}{m_{\mathrm{NO^+}}+m_n}}{\zeta_{\mathrm{NO^+}}} \tag{2.40b}$$

$$g_{\mathrm{NO^+}\perp} = \frac{\sum_n \frac{2m_{\mathrm{NO^+}}\nu_{\mathrm{NO^+}n}}{m_{\mathrm{NO^+}}+m_n}\left(\frac{1}{2}\frac{m_n}{k_b} - \frac{1}{6}\frac{m_n}{k_b}Q_{\mathrm{NO^+}n}\right)}{\zeta_{\mathrm{NO^+}}} \tag{2.40c}$$

$$g_{\mathrm{NO^+}\parallel} = \frac{\sum_n \frac{2m_{\mathrm{NO^+}}\nu_{\mathrm{NO^+}n}}{m_{\mathrm{NO^+}}+m_n}\frac{1}{4}\frac{m_n}{k_b}Q_{\mathrm{NO^+}n}}{\zeta_{\mathrm{NO^+}}} \tag{2.40d}$$

$$h_{\mathrm{NO^+O^+}} = \frac{\frac{6}{5}\frac{m_{\mathrm{NO^+}}\nu_{\mathrm{NO^+O^+}}}{m_{\mathrm{NO^+}}+m_{\mathrm{O^+}}}}{\zeta_{\mathrm{NO^+}}} \tag{2.40e}$$

$$k_{\mathrm{NO^+e^-}} = \frac{2\frac{m_{\mathrm{NO^+}}\nu_{\mathrm{NO^+e^-}}}{m_{\mathrm{NO^+}}+m_{\mathrm{e^-}}}}{\zeta_{\mathrm{NO^+}}} \tag{2.40f}$$

$$o_{\mathrm{NO^+O^+}} = \frac{\frac{4}{5}\frac{m_{\mathrm{NO^+}}\nu_{\mathrm{NO^+O^+}}}{m_{\mathrm{NO^+}}+m_{\mathrm{O^+}}}}{\zeta_{\mathrm{NO^+}}} \tag{2.40g}$$

$$\Delta_K = 1 - o_{\mathrm{O^+NO^+}}o_{\mathrm{NO^+O^+}} \tag{2.41}$$

Where ζ is given in Equation (2.42) below.

$$\zeta_{\mathrm{O^+}} = \sum_n \left[\frac{2m_{\mathrm{O^+}}\nu_{\mathrm{O^+}n}}{m_{\mathrm{O^+}}+m_n}\left(1+\frac{3}{4}\frac{m_n}{m_{\mathrm{O^+}}}Q_{\mathrm{O^+}n}\right)\right] + \frac{2m_{\mathrm{O^+}}\nu_{\mathrm{O^+NO^+}}}{m_{\mathrm{O^+}}+m_{\mathrm{NO^+}}}\left(1+\frac{3}{5}\frac{m_{\mathrm{NO^+}}}{m_{\mathrm{O^+}}}\right) + \frac{2m_{\mathrm{O^+}}\nu_{\mathrm{O^+e^-}}}{m_{\mathrm{O^+}}+m_{\mathrm{e^-}}}\left(1+\frac{3}{5}\frac{m_{\mathrm{e^-}}}{m_{\mathrm{O^+}}}\right) + \frac{6}{5}\nu_{\mathrm{O^+O^+}} \tag{2.42a}$$

$$\zeta_{\mathrm{NO^+}} = \sum_n \left[\frac{2m_{\mathrm{NO^+}}\nu_{\mathrm{NO^+}n}}{m_{\mathrm{NO^+}}+m_n}\left(1+\frac{3}{4}\frac{m_n}{m_{\mathrm{NO^+}}}Q_{\mathrm{NO^+}n}\right)\right] + \frac{2m_{\mathrm{NO^+}}\nu_{\mathrm{NO^+O^+}}}{m_{\mathrm{NO^+}}+m_{\mathrm{O^+}}}\left(1+\frac{3}{5}\frac{m_{\mathrm{O^+}}}{m_{\mathrm{NO^+}}}\right) + \frac{2m_{\mathrm{NO^+}}\nu_{\mathrm{NO^+e^-}}}{m_{\mathrm{NO^+}}+m_{\mathrm{e^-}}}\left(1+\frac{3}{5}\frac{m_{\mathrm{e^-}}}{m_{\mathrm{NO^+}}}\right) + \frac{6}{5}\nu_{\mathrm{NO^+NO^+}} \tag{2.42b}$$

2.4.1 Collision Effects on Temperature

The following two figures, Figures 2.4 and 2.5, illustrate the collisional effects on possible temperature profiles. The profile synthetic datasets are made with the following parameters: F10.7a is 164.5; F10.7 is 132.2; ap is 10; ap3 is 10; UT is 3; altitude profile is 90 to 500 km; date is 26 February 2001; latitude is 67^o (Sondrestrom) to 68^o; longitude is 309^o (Sondrestrom) to 310^o; chapman function is used to generate electron density profile; and, z_c is assumed to be 210. Figure 2.4 shows how electric fields (top two panels) and electron temperatures (bottom two panels) affect the profiles with fixed electric field values of 50 $^{\mathrm{mV}}/_{\mathrm{m}}$ for E_x and E_y for the bottom two panels. The top two panels illustrate the effects of increasing electric field values which has a direct relationship to increasing the average temperature, defined as $T_{avg_s} = \frac{1}{3}T_{s\parallel} + \frac{2}{3}T_{s\perp}$. The bottom two panels show how electron temperatures affect the green curves (50 $^{\mathrm{mV}}/_{\mathrm{m}}$) in the top two panels: electron temperature, densities, and thus Coulomb collisions become important above about 250 km. Figure 2.5 shows how varying electric field values affect the components of the top two panels of Figure 2.4's profiles with an electron temperature equal to the neutral temperature (1000 K). The left two panels add to the average O^+ temperature and the right two panels add to the average NO^+ temperature, as given above. Below 350 km, the perpendicular temperatures are larger than the parallel temperatures if the electric field values are greater than 25 $^{\mathrm{mV}}/_{\mathrm{m}}$. An interesting feature is the $T_{O^+\parallel}$ temperature decrease for large electric fields (> 50 $^{\mathrm{mV}}/_{\mathrm{m}}$). This is due to the perpendicular temperature thermalizing from coulomb collisions into the parallel temperature through Equations (2.24), (2.35), and (2.36). It is noted that there is a large wind shear at about 200 km from the HWM output for the above parameters.

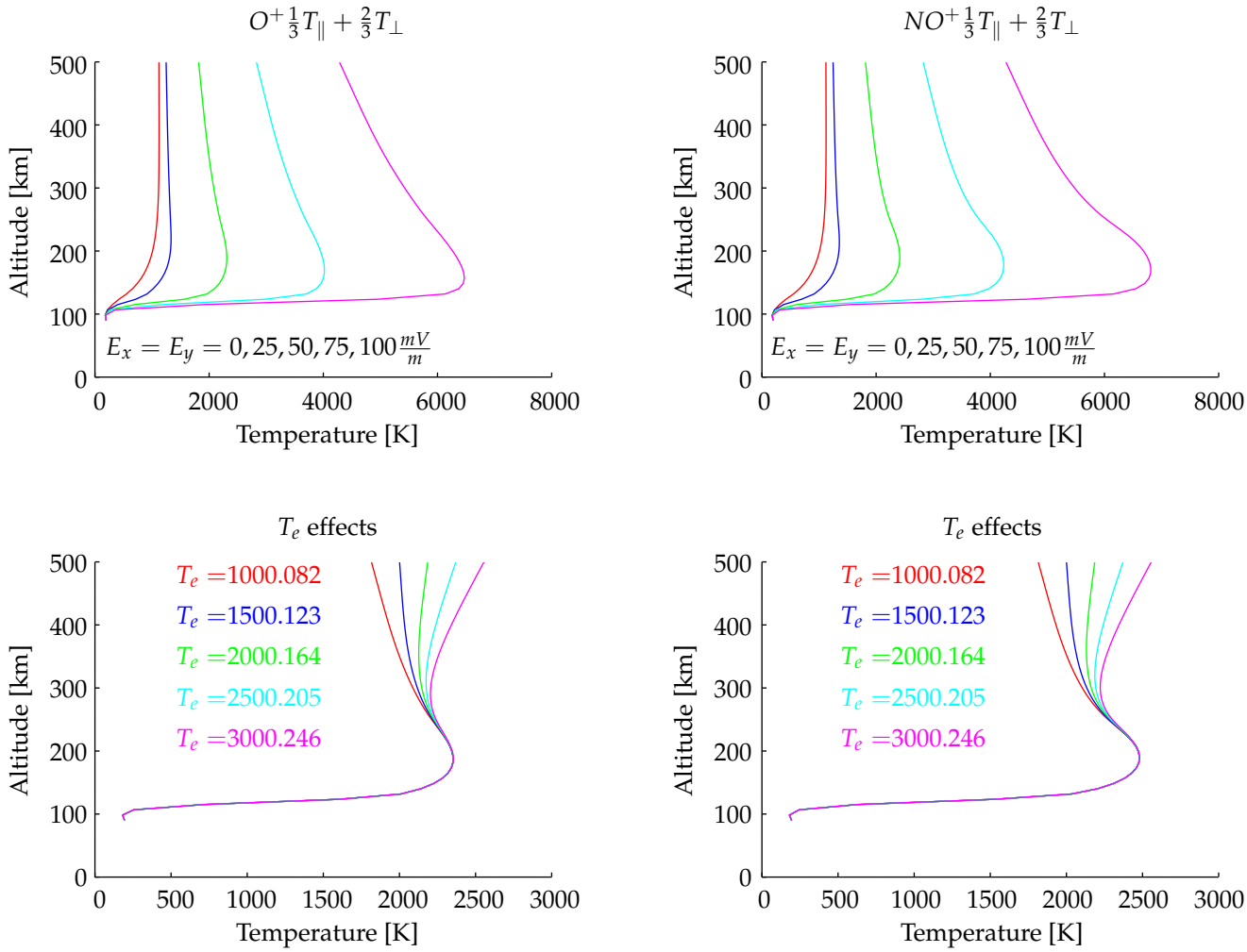

Figure 2.4: Electric field and electron temperature dependencies of ion temperatures. The electric field values for the bottom two plots are 50 $^{\mathrm{mV}}/_{\mathrm{m}}$.

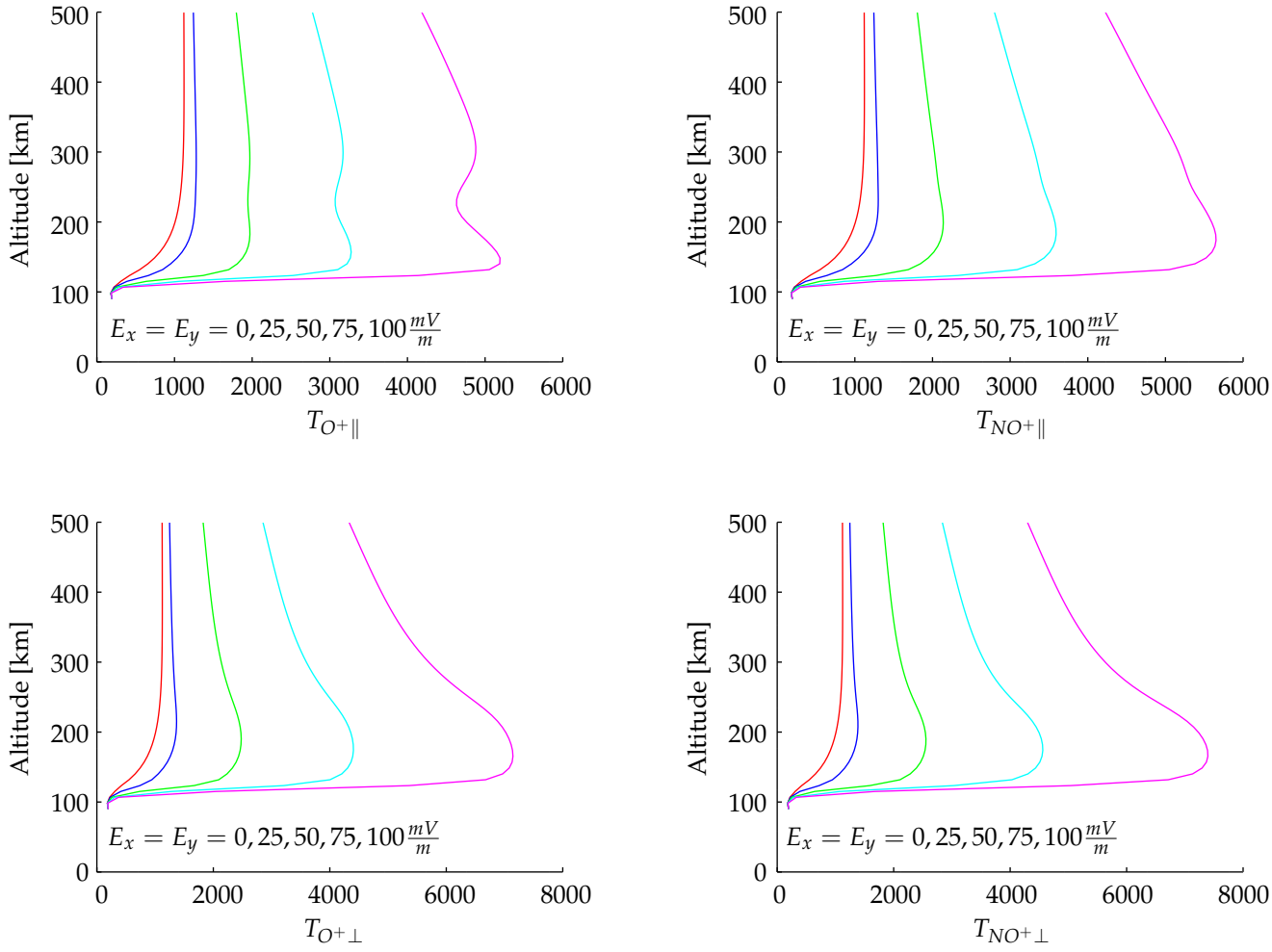

Figure 2.5: The solution of the pressure tensor gives the parallel and perpendicular ion species temperatures as seen above for various electric field values.

2.5 Recap: Procedure of Estimation

Using Model A, B, or C, calculate the O^+ and NO^+ parallel and perpendicular temperatures. Input those temperatures into Equation (2.8) to get the O^+ and NO^+ line-of-sight temperatures. These ion specific line-of-sight temperatures are then input into Equation (2.7). This temperature is now known as T_{model}. Use Equation (2.6) to estimate, in a least squares sense, the ion composition p, the crossover altitude z_c, and the electric field $\boldsymbol{E}_\perp$ (effective electric field $\boldsymbol{E}'_\perp$ for Model A). This is done for the altitude range of 100 to 500 km. The fitter constrains these values in the following way: z_c is between 140 and 500 km; H is between 10 and 50 km; and electric fields are between -250 and 250 $^{\mathrm{mV}}/_{\mathrm{m}}$.

2.6 Error Checking: Determination of Bad Fits

Occasionally, the fitting algorithm does not work very well. In order to automatically detect these incidents, the following error checking routines were implemented. If the following limits are true, the fit is considered bad. If z_c is either 140 or 500 km AND H is either 10 or 50 km the fit is considered bad. That is, if the fitter hits two constraining values, the fit is considered bad. The fit is also considered to be bad for these 2 cases: if the standardized residual, the residual divided by the standard deviation, is greater than 2 for at least 2 points in the altitude range of 130-500 km; and, if the residual is greater than 500 K or less than -500 K for at least 2 points in the altitude range of 120-500 km. These limits were determined qualitatively.

Chapter 3

Results: Case Studies at Sondrestrom

The datasets used are from the Sondrestrom Upper Atmospheric Research Facility ISR in Kangerlussuaq, Greenland. The ISR features a fully steerable antenna along with a low noise amplifier, receivers, and digital signal processing computers. The Geomagnetic storms and quiet datasets are looked at. The geomagnetic storms for this study satisfy the following requirement: $K_p > 4$ for at least 4 consecutive hours. The quiet datasets for this study satisfy the following requirement: $K_p \leq 2$ for all times, often 0. Table 3.1 lists the datasets used.

Sondrestrom Datasets					
Storm			Quiet		
26	August	1998	12	March	2006
07	October	2002	13	March	2006
27	May	2003	23	March	2006
28	October	2003	31	March	2006
11	November	2003	01	April	2006
20	November	2003	20	March	2007
09	November	2004	12	April	2007
24	May	2007	07	June	2007
27	September	2007	19	July	2007
28	February	2008	11	October	2007
27	March	2008	06	December	2007
			03	October	2008
			31	July	2008
			16	October	2008
			13	November	2008
			18	December	2008

Table 3.1: The storm and quiet datasets used in this study. There are 11 storm datasets and 16 quiet datasets.

3.1 Temperature Profile Examples

This section shows temperature profiles for the radar and fits resulting from all 3 models which highlights some differences in the models. The below 10 temperature profile examples have the following format: the top left panel is Model A; the middle left panel is Model B; the middle right panel is Model C; and, the bottom panel is a comparison of the composition and scale heights for the radar and models. All the plots are compared to altitude on the vertical axis. The Model A panel shows the radar ion temperature in red, the O^+, NO^+, and total ion temperature produced from utilizing Model A in blue, the model temperature with radar assumed composition in green (as mapped using the Waldteufel functions,

see Equations (2.3), (2.4), and (2.5)), $E'_{\perp}$, and z_c. The Model B and C panels show similar output along with the altitude dependent neutral wind speeds, the average wind speed, $|E_{\perp}|$ and average $|E'_{\perp}|$. All model panels show z_c as a horizontal black line. The bottom panel shows how p varies with altitude along with H values for the models (Model A has a static scale height of 30 km). In general, a fit can be considered good if the green line, the modeled temperature, matches well with the red line, the ISR temperature data, since the least squares minimization procedure minimizes the residuals of these two temperature profiles.

Figure 3.1 shows how the models fit the quiet portion of the dataset for 28 February 2008 at 1:08.84 UT. The variation between the models of the temperature profile (blue) is indistinguishable, especially considering all the ISR variables have associated error values. However, the models all fit this profile while estimating slightly different composition parameters. Model A estimates larger z_c and $E'_{\perp}$ values than Models B and C. The Scale height is lower for Models B and C than for Model A and the ISR. It is noted that above 350 km, ISR temperature errors become large. The ion species show the same temperature due to small electric field values. Similar analysis of other data produces essentially identical results.

Figures 3.3, 3.4, 3.5, 3.6, 3.7, and 3.8 show how the models fit heating events in the ionosphere. These heating events are characterized by the radar temperature profile (red) having an artificial inversion typically between 150 and 300 km. This inversion is unphysical and is a sign of incorrect fitter composition as discussed in, e.g., Zettergren et al. [2010]. The aforementioned examples are intended to show a range of possible heating situations and showcase the successes and limitations of the fitting procedure.

Figure 3.3 is a moderate-to-weak heating event for 10 March 1998 at 11:34.44 UT. As $E'_{\perp}$ increases, so does z_c, with Model C's $E'_{\perp}$ and z_c values halfway between the Model A and B values. The crossover altitude increasing as $E'_{\perp}$ increases is consistent with ion frictional heating increasing the ion temperature which then increases NO^+ through Reaction (1.1). It is also noted that Model C best fits the data, noticeably above 300 km.

Figure 3.4 is a weak-to-moderate heating event for 10 March 1998 at 11:35.46

UT. Models B and C fit the data better than Model A, and both have lower z_c and $E'_\perp$. Models B and C have similar z_c yet different $E'_\perp$ due to the very large zonal wind values along with Equations (2.24) and (2.30) which differentiate the models' O^+ and NO^+ temperatures. This ion temperature difference is most notable above 250 km, consistent with Section 2.4.1.

Figure 3.5 is a heating event for 10 March 1998 at 11:42.54 UT. Model A adds NO^+ into the high altitudes in order to fit the radar data there, thus causing z_c and $E'_\perp$ to be large. This is likely a limitation of not including Coulomb collisions. Models B and C fit the data in opposite ways as can be seen by their z_c and H values. Considering Model B's H hits the fitter boundary, Model C is the more realistic fit and expands upon the heating theme in the previous time steps as seen in Figures 3.3 and 3.4. Model C fits the data better than Model A, as seen in the residuals between their respective radar and model mapped to radar temperatures, the red and green lines, respectively. Also, Model B's solution is unlikely due to Reaction (1.1) favoring conversion of O^+ to NO^+ during heating events, yet Model B has a low z_c, causing 40% of the ion population to be O^+ at 100 km!

Figure 3.6 is a heating event for 10 March 1998 at 11:43.56 UT. Models A and B fit the data very similarly, using the same z_c but Model A has $E'_\perp$ being 20 $^{\mathrm{mV}}/_{\mathrm{m}}$ larger than model B. Model C uses a large z_c and $E'_\perp$ in order to better fit the higher altitude data. Since Model B and C both have small residuals throughout the altitude profile yet fit different $\boldsymbol{x}_{est}$, it is ambiguous whether Model B or Model C is the better fit. Model B has a better fit below 250 km, while Model C has a better fit above 250 km which is where collisions and electron temperatures become important (see Section 2.4.1). Consideration of Figure 3.5, which occurs 1 minute prior, shows a temperature difference of 300 K for Model B. Also, as discussed later, Model C's scale height is below 30 km, which is typical for the daytime.

Figure 3.7 is a heating event for 7 October 2002 at 00:30.55 UT. All models fit the data well and correct the temperature inversion. Model C outperforms Models A and B by having smaller residuals for more altitude points. Model B shows vast differences in species temperatures starting at 150 km with NO^+ heating to about 2200 K. This is not seen in Model C most likely due to cross species ion-ion

collisions which are not modeled in Model B.

Figure 3.8 is a heating event for 7 October 2002 at 2:16.16 UT. Model B underestimates the temperature profile and assumes a low altitude (small z_c), spread out (large H) transition into O^+ which is unlikely for a heating event due to Reaction (1.1) which states that heating causes conversion of O^+ into NO^+. Models A and C both fit the data well, with Model C outperforming model A as seen by smaller residuals throughout the profile (difference between green and red lines), especially from 225-300 km, where electron temperatures begin to have a noticeable effect on ion temperatures (see, e.g., Figure 2.4.1).

Figures 3.9, 3.10, and 3.11 are examples of bad fits to the radar data as defined in Section 2.6. Figure 3.9 Model C and Figure 3.10 Model C exemplify the fitter "hitting the rails" for both H and z_c. Figure 3.10 Model B and Figure 3.11 Model B exemplify temperature residuals that are too large. From the few examples shown above, Model C often qualitatively outperformed Models A and B. More importantly, across the aggregate number of badfits for the datasets in Table 3.1, Model C has the least amount of badfits.

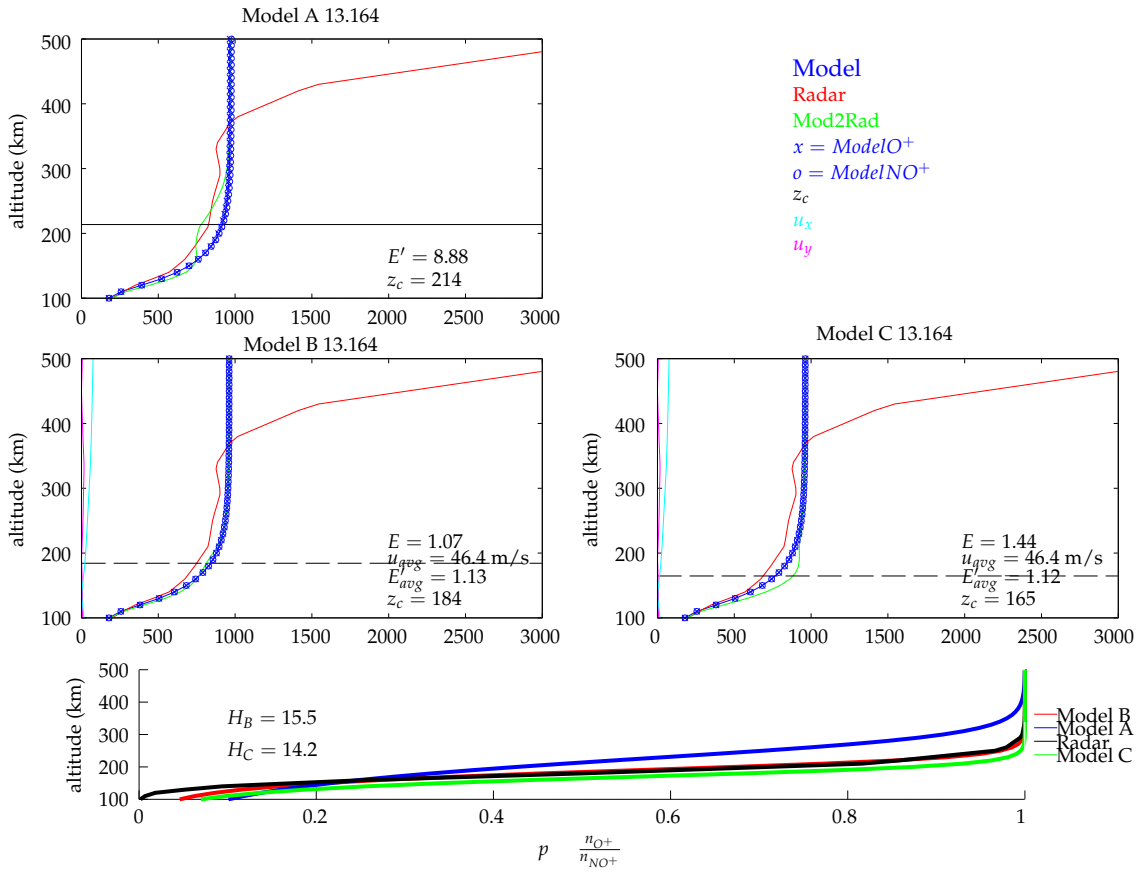

Figure 3.1: A calm time period for 28 February 2008 at 1:08.84 UT. All models fit the data well up to 350 km where the radar temperature errors become large. Model A estimates the largest z_c.

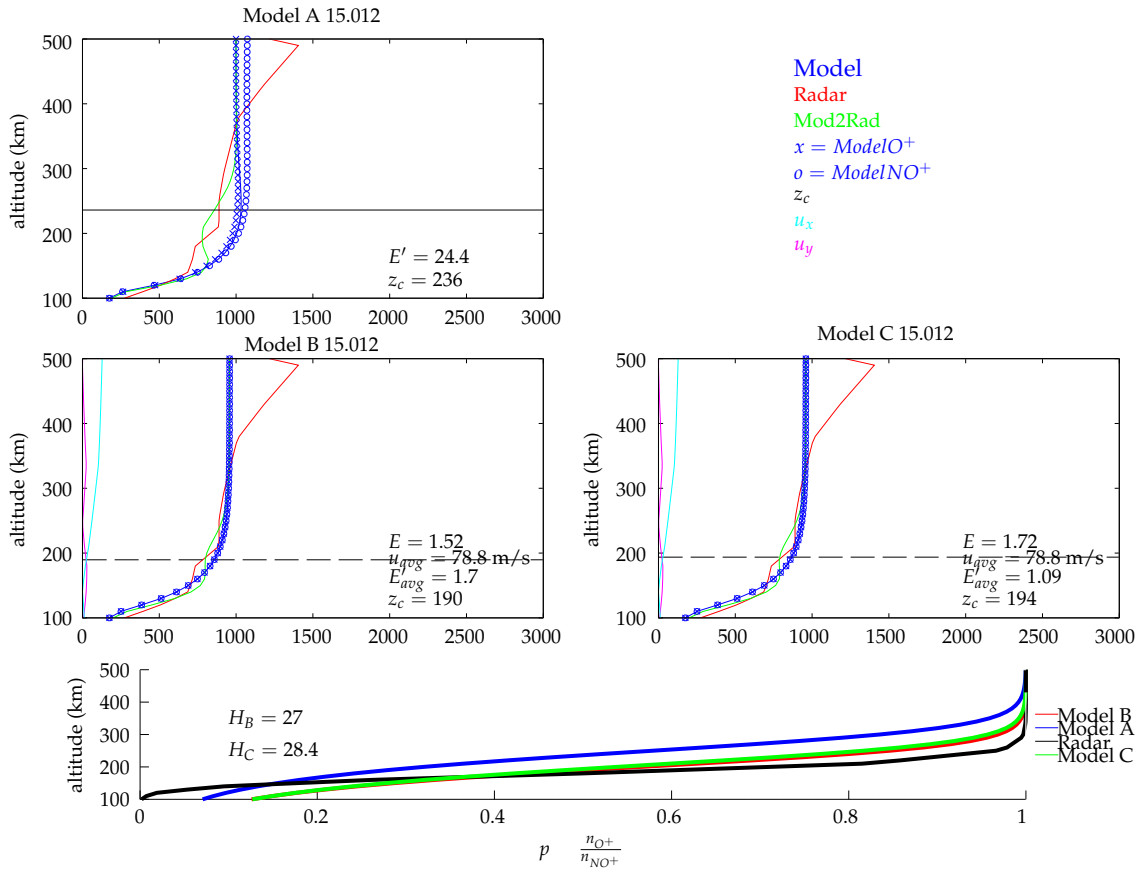

Figure 3.2: A calm time period for 28 February 2008 at 3:00.72 UT. Models B and C fit the data extremely well with very similar parameters. Model C unnecessarily increases z_c and $E'_\perp$, and thus the temperature.

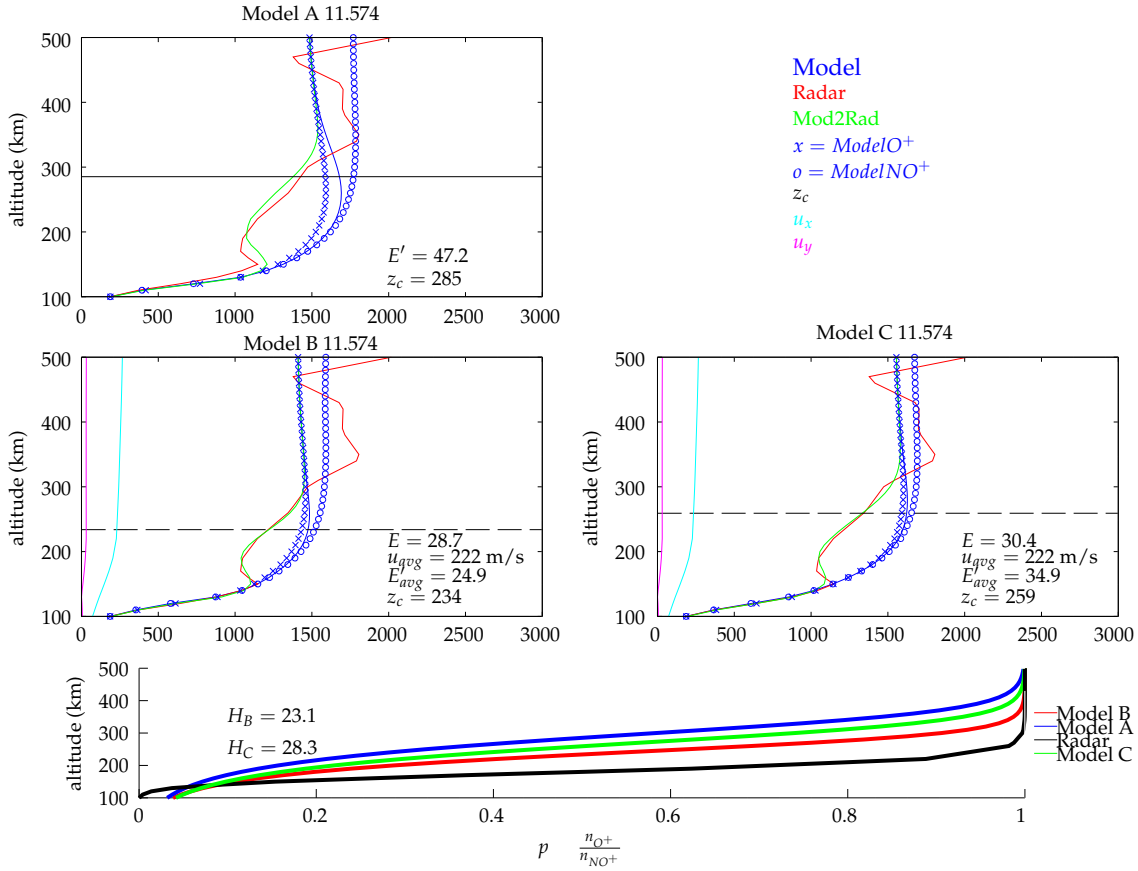

Figure 3.3: A heating event for 10 March 1998 at 11:34.44 UT.

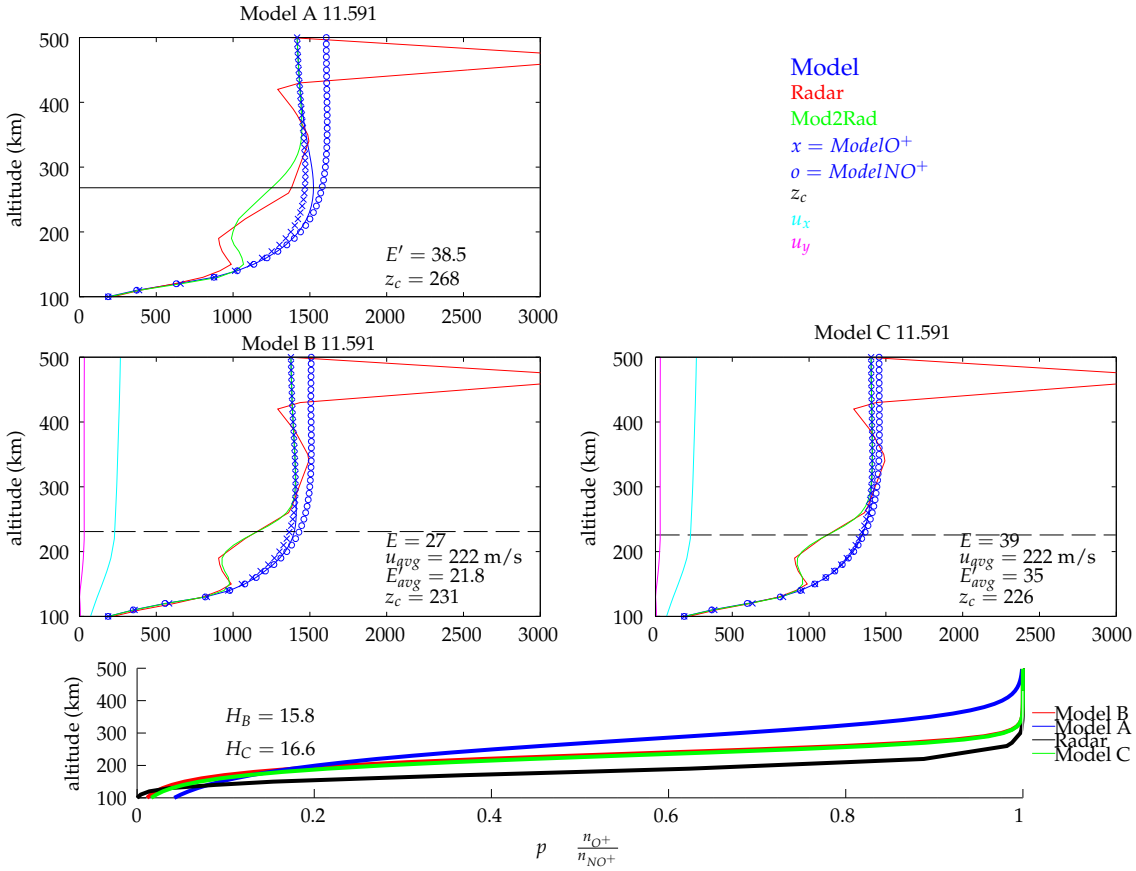

Figure 3.4: A heating event for 10 March 1998 at 11:35.46 UT.

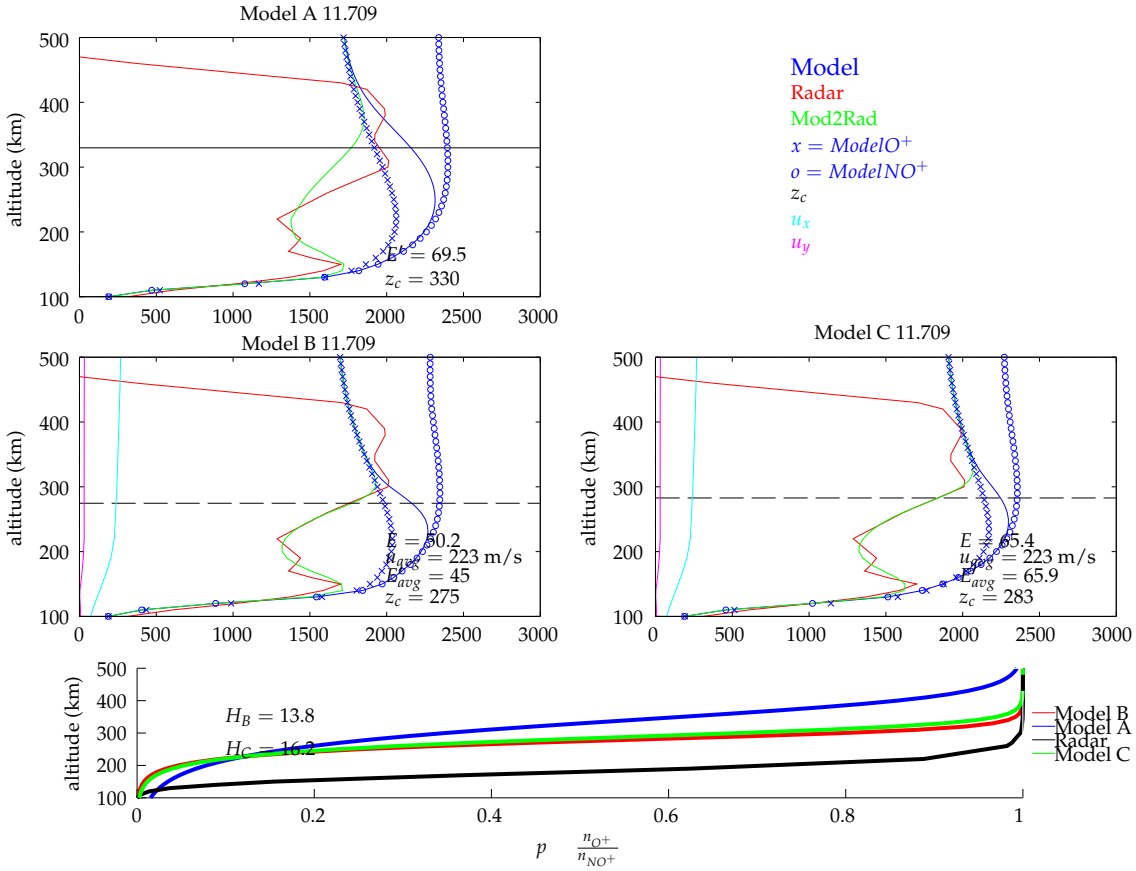

Figure 3.5: A heating event for 10 March 1998 at 11:42.54 UT.

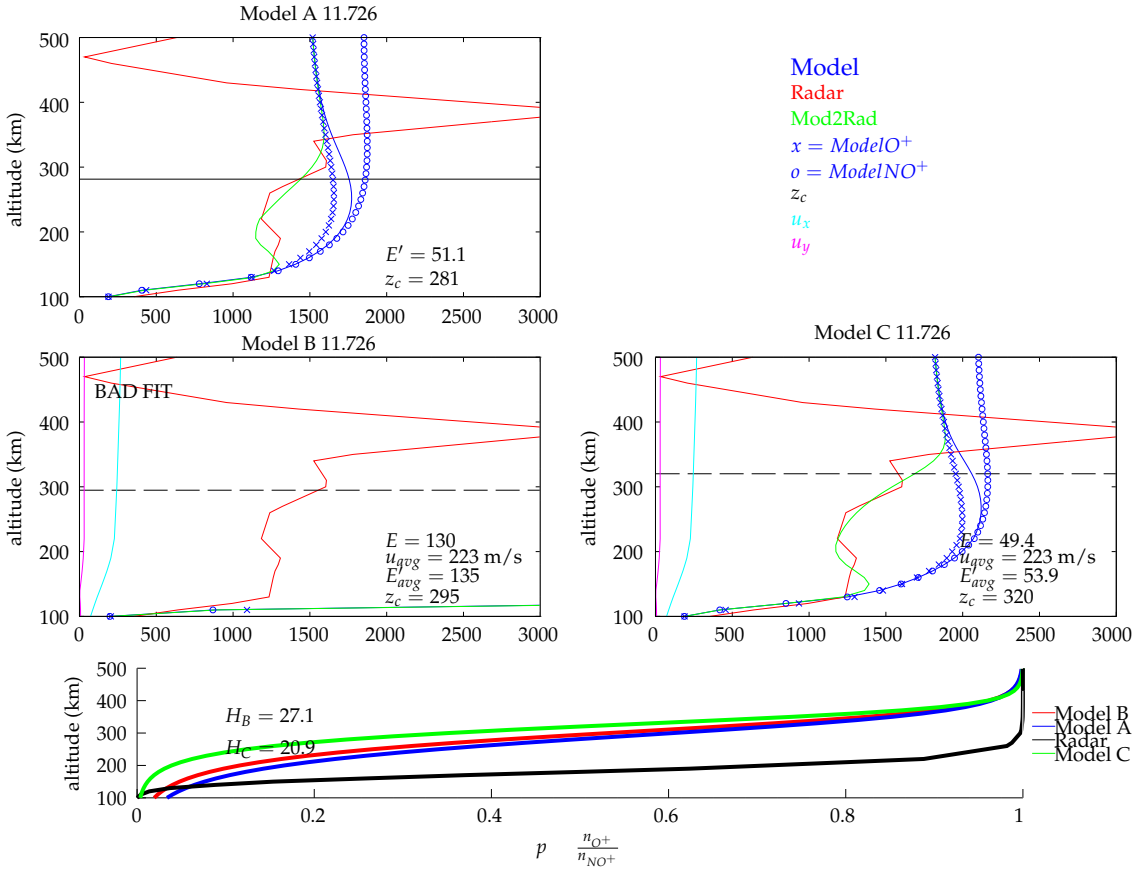

Figure 3.6: A heating event for 10 March 1998 at 11:43.56 UT.

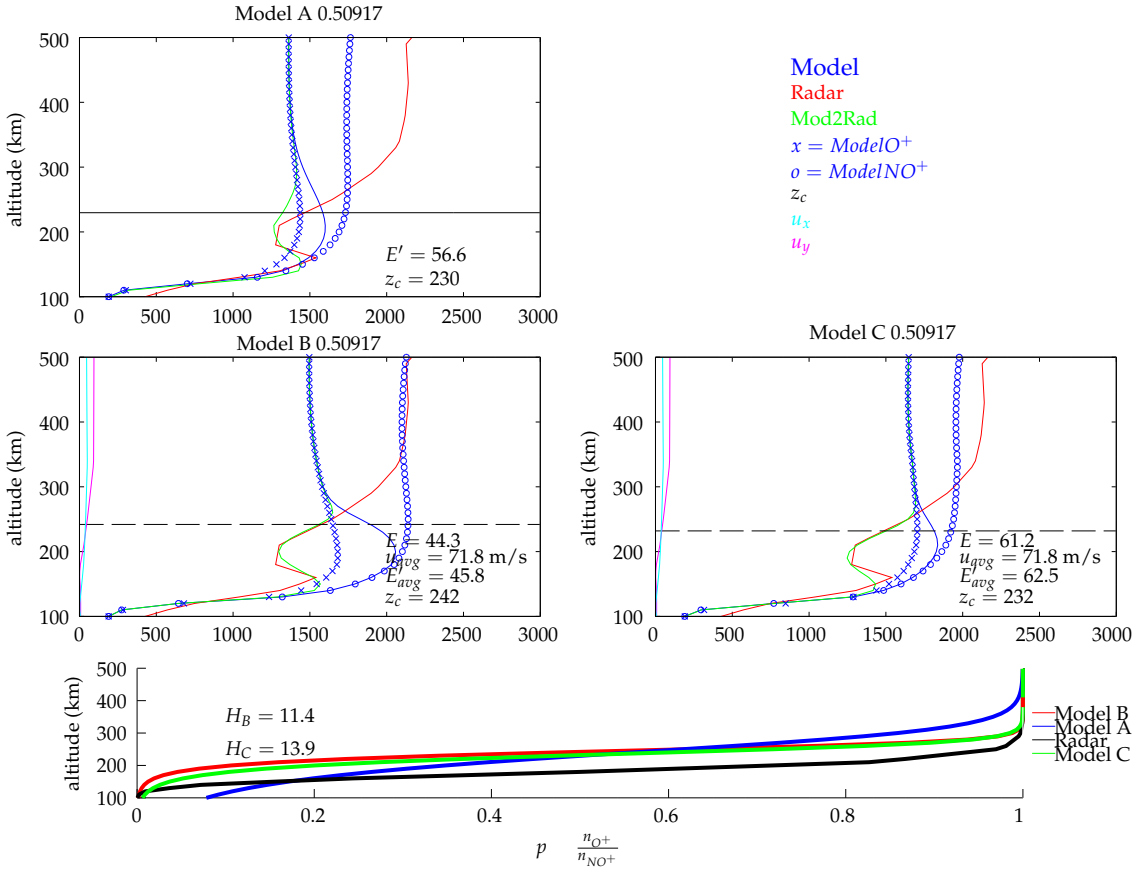

Figure 3.7: A heating event for 7 October 2002 at 00:30.55 UT.

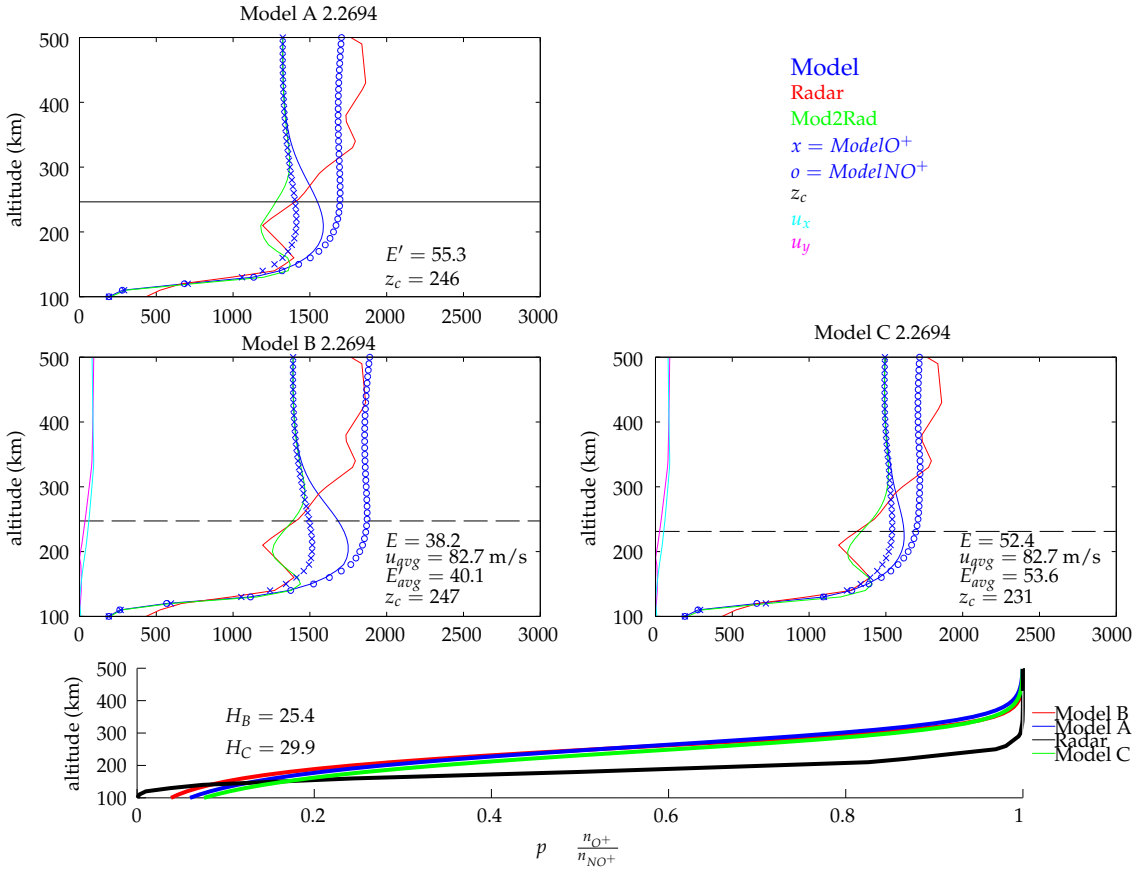

Figure 3.8: A heating event for 7 October 2002 at 2:16.16 UT.

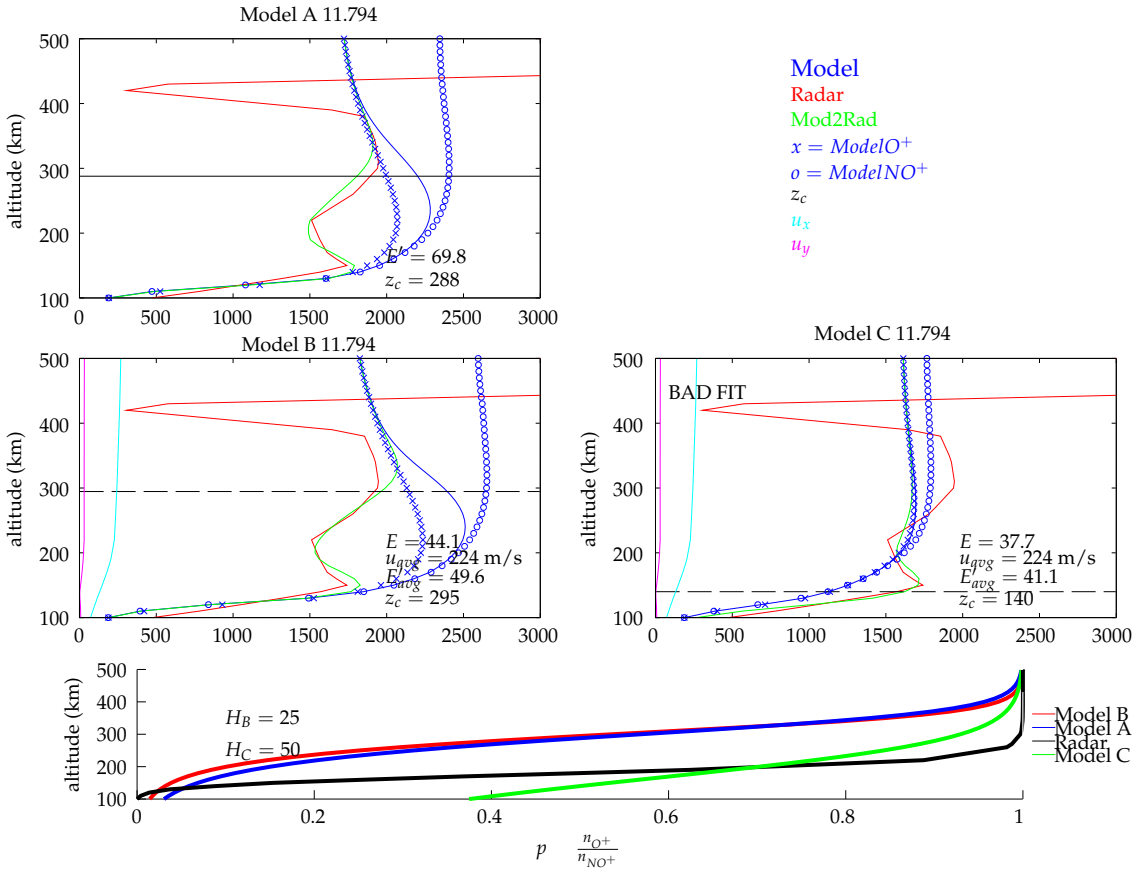

Figure 3.9: A heating event for 10 March 1998 at 11:47.64 UT. Models A and B both fit the radar data well, however Model B gives significantly lower estimates for z_c and $E'_{\perp}$. Model C gives an example of a bad fit as H and z_c hit the fitter rails as described in Section 2.6.

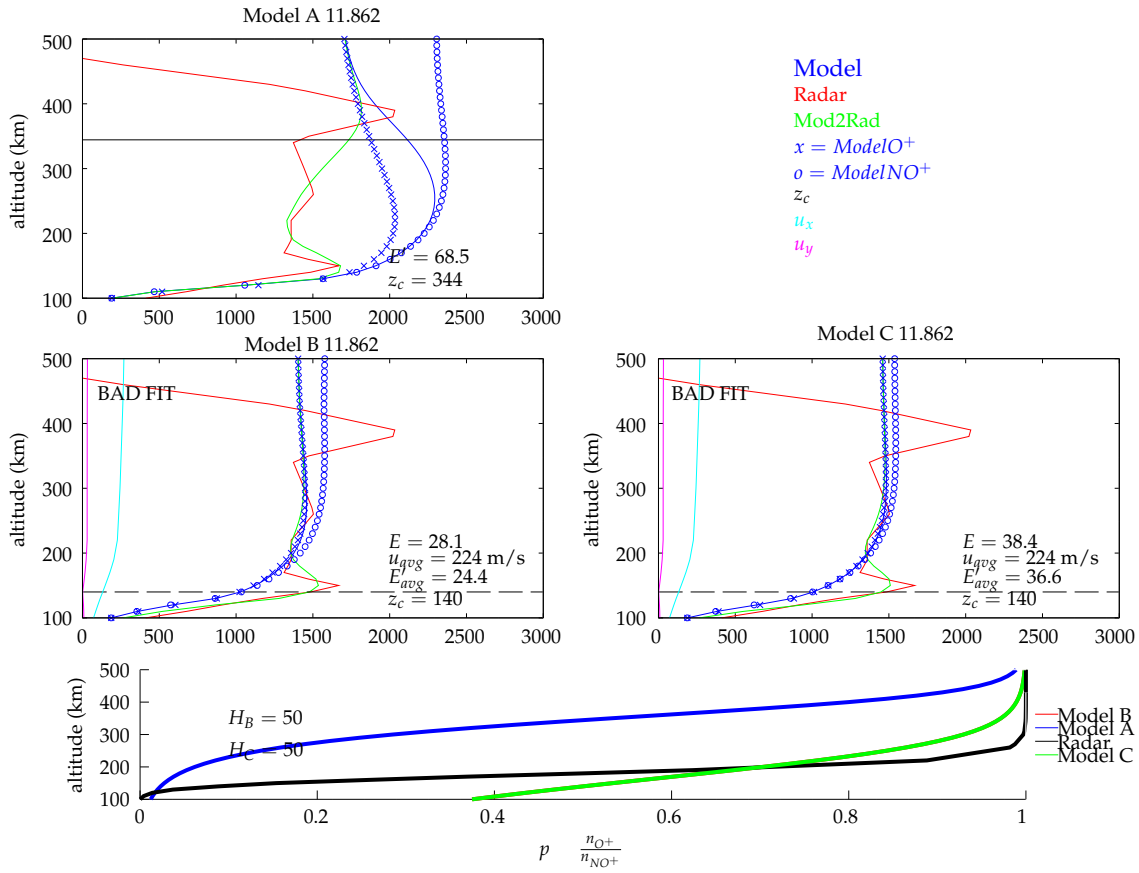

Figure 3.10: A heating event for 10 March 1998 at 11:51.72 UT. Model A fits the radar data but with large quantities of high altitude NO^+. Model B and C both meet the bad fit criteria as described in Section 2.6.

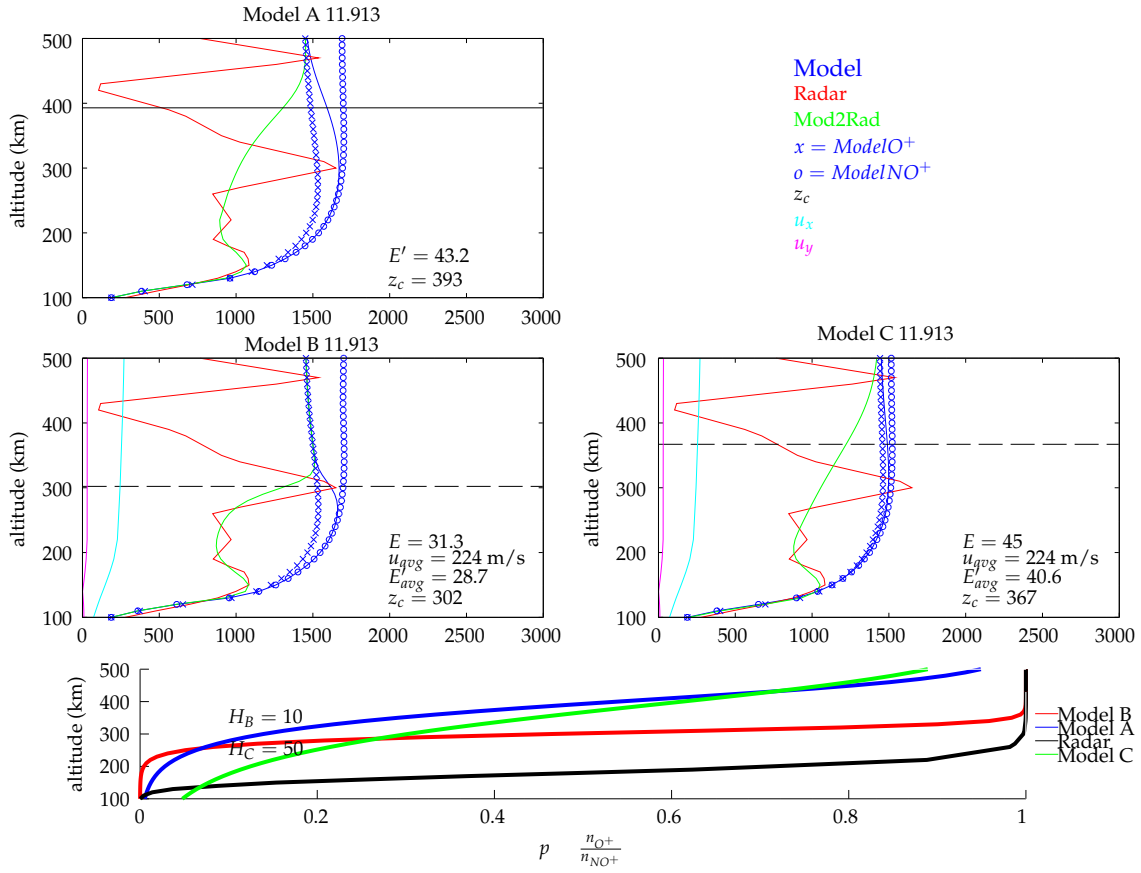

Figure 3.11: A heating event for 10 March 1998 at 11:54.78 UT. Models A and C both fit the data well while estimating very large z_c's. However, Model C fits the radar data better above 250 km which is where collisions start to make a large difference as seen in Figure 2.4. Model B gives an example of a bad fit as described in Section 2.6.

3.2 Neutral Wind Effects, Parameter Estimation, and 11 November 2003 Case Study

The effects of neutral winds on Models A and B are discussed along with sequential versus simultaneous parameter estimation (A versus B). Also discussed are correlations of composition parameters. The storm datasets from 11 November 2003 and 26 August 1998 are used. Letting $u_\perp = 0$ is equivalent to estimating $E'_\perp$ instead of estimating E_x and E_y since $\boldsymbol{E}'_\perp = \boldsymbol{E}_\perp + \boldsymbol{u}_\perp \times \boldsymbol{B}$.

In Figure 3.12 below, Models A and B for the 11 November 2003 storm dataset are used. These plots compare running Model B with winds (red) and with $u_\perp = 0$ (blue) along with Model A (green). Model A implicitly estimates neutral wind effects by estimating $E'_\perp$ while Model B explicitly estimates neutral wind effects by using HWM wind field output and estimating $\boldsymbol{E}_\perp$. The effective electric field shows little change between Model B variants, however, Model A's $E'_\perp$ has larger and more frequent spikes. There is a clear trend with z_c between the models: Model A estimates larger altitudes than Model B with explicit winds (red) which in turn estimates larger altitudes than Model B with implicit winds (blue). This is also due to Model B adjusting H in the fitter to better fit z_c. Model A estimating the larger values for effective electric field and crossover altitude is consistent with there being a direct relationship between the two. Although B with implicit winds estimates lower z_c, it estimates a larger H than B with explicit winds. Comparing the B models (explicit versus implicit), it is shown that the explicit inclusion of winds acts to slightly raise the crossover altitude but make the transition from NO^+ to O^+ in a smaller altitude region (H comparison).

Comparison of Model A and Model B with implicit winds at points where the scale height are the same (30 km) gives an understanding of sequential versus simultaneous parameter estimation for the temperature fits. The sequential fit, estimating $E'_\perp$ in the E region (130-150 km) and then estimating z_c, leads to larger values of z_c and $E'_\perp$ than when the parameters are estimated simultaneously. A possible reason for this is that there are only 1-3 (usually 1) independent measurements from the ISR at this altitude. The three interpolated data points (at 130, 140,

and 150 km) constitute a much smaller least squares fitting range than for Model B, which uses 100 - 500 km as the fitting range. However, above 350 km, the ISR temperature measurements errors are much larger, and are thus weighted accordingly. Still, that is, in general, at least 26 good data points compared to 3.

In Figure 3.12, there is correlation between the peaks of z_c and $E'_\perp$ when the dataset is not disturbed for long periods of time. At about 22, 105 and 120 hours since experiment start, local maximums of z_c and $E'_\perp$ coincide with each other. When there is extended geomagnetic activity, as is seen by $K_p > 5$ for 40 to 80 hours since the experiment start (bottom panel), this correlation disappears, which is seen from to 80. Also of interest is that scale height correlates with crossover altitude: as moleculars are pushed higher into the atmosphere, the transition to O^+ becomes more and more spread out with respect to altitude. This result is intuitive since as altitude increases, density decreases, and thus reactions rates are reduced, allowing for longer NO^+ lifetimes. It is interesting that when there is a lack of correlation between the z_c and $E'_\perp$ peaks, as described above, the wind fields at HMF2, the altitude at which the ion density is a maximum in the F region, are greatly disturbed from their diurnal trends, as seen in the bottom panel of Figure 3.12. The z_c and $E'_\perp$ correlations are further corroborated by Figure 3.13 below which scatter plots z_c as a function of $E'_\perp$. It is seen that z_c increases as $E'_\perp$ increases, as expected from Reaction (1.1). The vertical axis intercepts for Figure 3.13 vary between B with $\boldsymbol{u}_\perp = 0$ having 218, Model A having 226,and Model B having 234 km. This suggests, that at low effective electric field values, the neutral winds play an important role in z_c estimation due to them contributing more significantly to $E'_\perp$ through $\boldsymbol{u}_\perp \times \boldsymbol{B}$.

Letting $\boldsymbol{u}_\perp = 0$ for Model B allows a comparison between procedural estimation and simultaneous estimation techniques, Models A and B (also C), respectively. In Figure 3.14 below, which correspond to Figure 3.3 above, Model A is compared with Model B when $\boldsymbol{u}_\perp = 0$. It is shown that z_c, H, and $E'_\perp$ are all lower when the parameters are estimated simultaneously. Juxtaposition of the figure pair, Figures 3.3 with 3.14, it is seen that implicit wind estimation leads to higher

estimates of z_c, H, and $E'_{\perp}$ compared with the explicit values found with the assistance of the HWM. This appears to be the case for many other datasets we have examined.

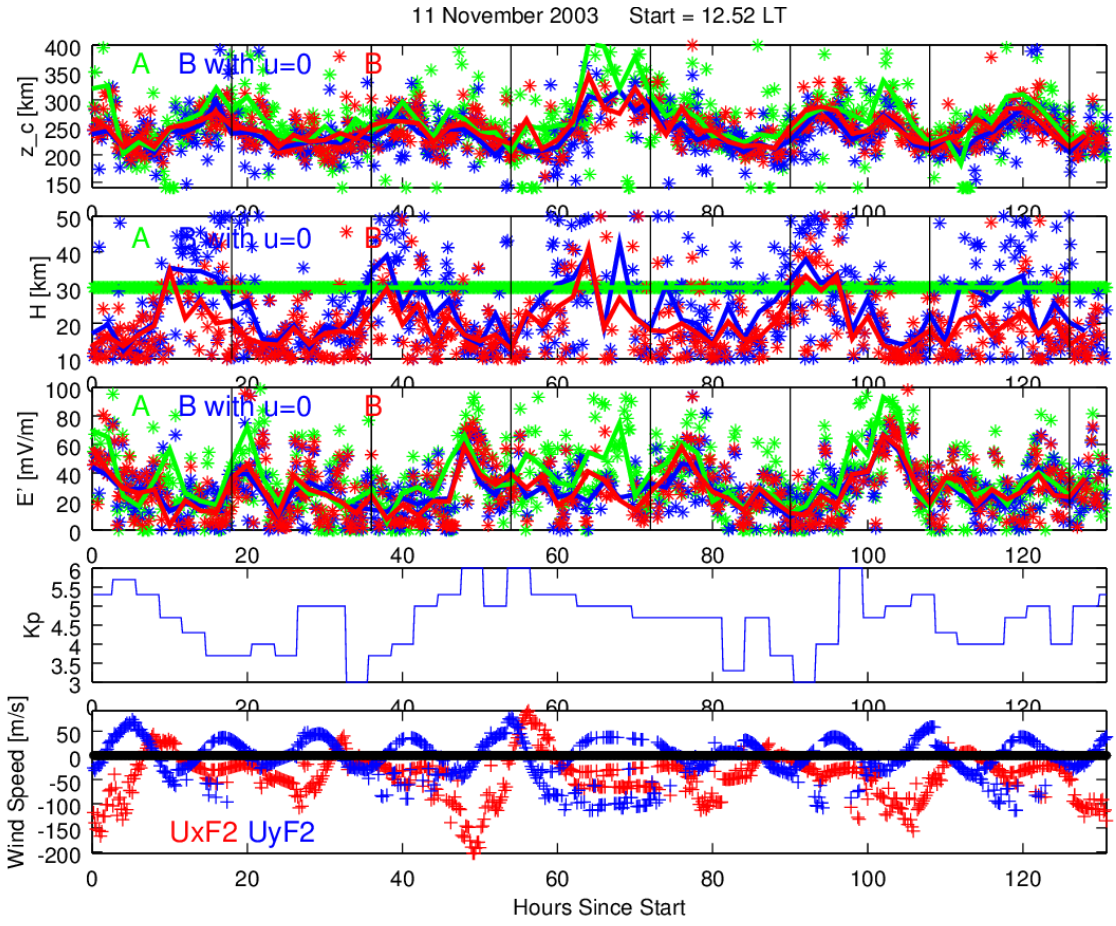

Figure 3.12: Model A and Model B, with and without explicit inclusion of neutral winds, for the 11 November 2003 storm dataset are juxtaposed along with geomagnetic activity. The vertical black lines indicate 6:30 am LT.

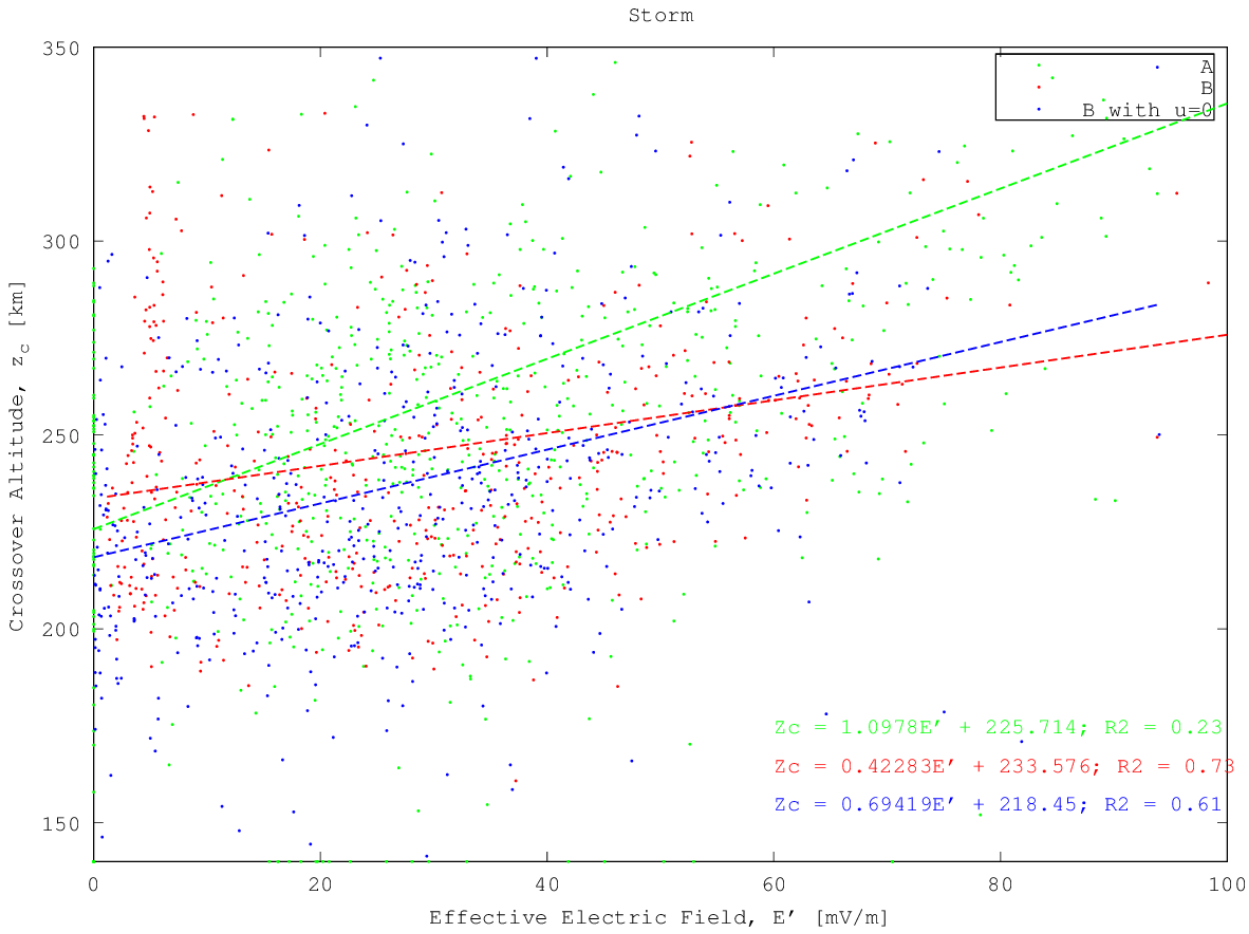

Figure 3.13: The correlation between effective electric field and crossover altitude for the data in Figure 3.12 above.

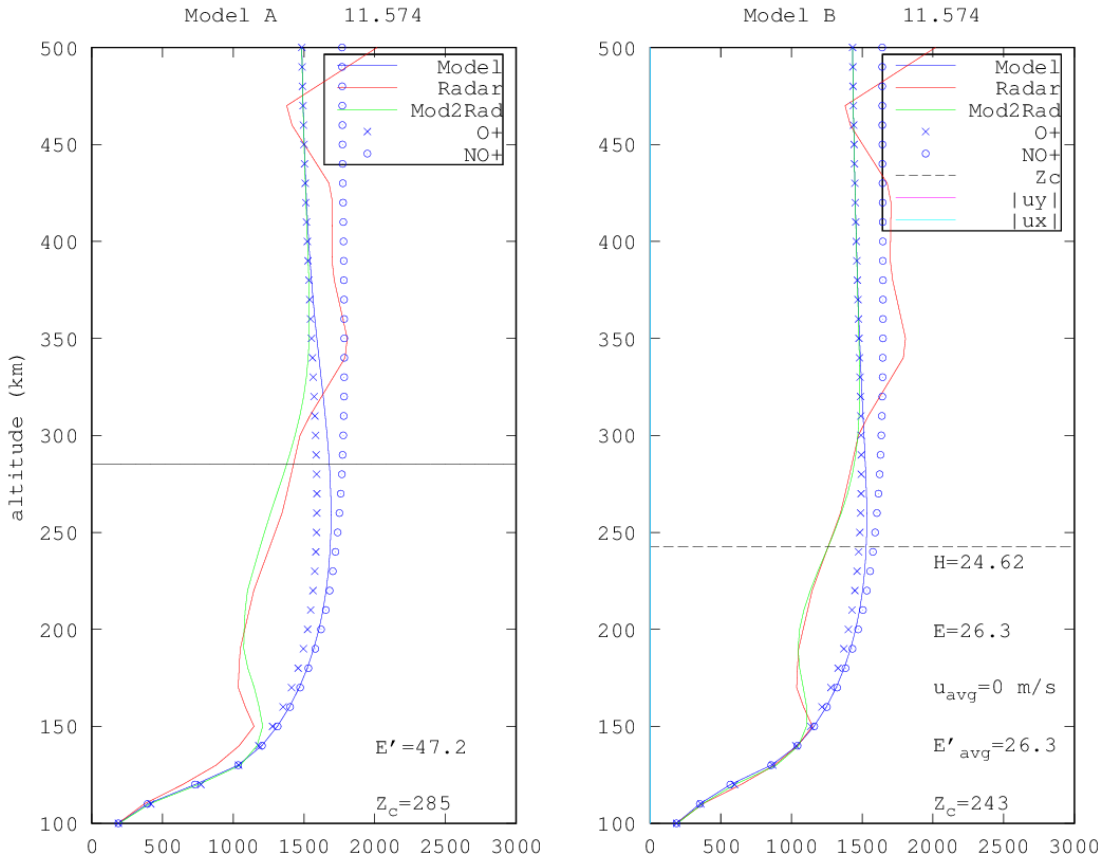

Figure 3.14: A heating event for 10 March 1998 at 11:34.44 UT. Models A and B are compared when they both implicitly estimate $\boldsymbol{u}_\perp \times \boldsymbol{B}$ by letting $u_\perp = 0$ for Model B. All parameters are lower for Model B which simultaneously estimates the parameters. See also Figure 3.3.

3.3 27 May 2003 Storm Case Study & 23 March 2006 Quiet Case Study

The figures below represent storm (Figures 3.15 and 3.16) and quiet time (Figures 3.17 and 3.18) typical conditions.

In Figure 3.15, z_c peaks are well correlated in time with $E'_\perp$ peaks at x-axis values of about 15, 43, and 50. Once geomagnetic activity is sustained for over 10 hours (i.e. 48-65 hours since start) the z_c and $E'_\perp$ peak correlation no longer holds. Model B and C crossover altitudes are in close agreement whereas Model A consistently estimates larger values. Similarly for $E'_\perp$. Scale heights for Models B and C are very similar except after sustained geomagnetic disturbances greater than 5 K_p (60-75 hours since start). Figure 3.16 corroborates the above relation between z_c and $E'_\perp$ peaks: as $E'_\perp$ increases, so does z_c for previously discussed reasons.

In Figure 3.17, it is seen that z_c is often near 200 km, with increases during the nighttime up to about 250 km. H and $E'_\perp$ follow likewise trends. Model A estimates, on average, larger crossover altitudes and effective electric fields compared to Models B and C. The electric field values are often below 20 $^{\mathrm{mV}}/_{\mathrm{m}}$, which do not produce significant ion heating (see Figures 2.4 and 2.5). Figure 3.18 shows that z_c increases as $E'_\perp$ increases for the quiet dataset. This is consistent with the nighttime increases of z_c and $E'_\perp$ in Figure 3.17.

3.3.1 Quiet versus Storm Variations

Comparing the two datasets above, we can draw some preliminary correlations regarding quiet versus storm time trends. These correlations will be expanded upon in the next chapter, in which all of the storm and quiet datasets are combined into 2 large datasets, one for storm times and one for quiet times. The crossover altitude increases by about 30 km during storm times. Model A estimates larger z_c and $E'_\perp$ values for quiet and storm times. For quiet and storm times, $\boldsymbol{x}_{est}$ is lower during daytime. Crossover altitude increases correlated with geomagnetic activity level increases findings are consistent with Litvin et al. [1998]'s findings of mid

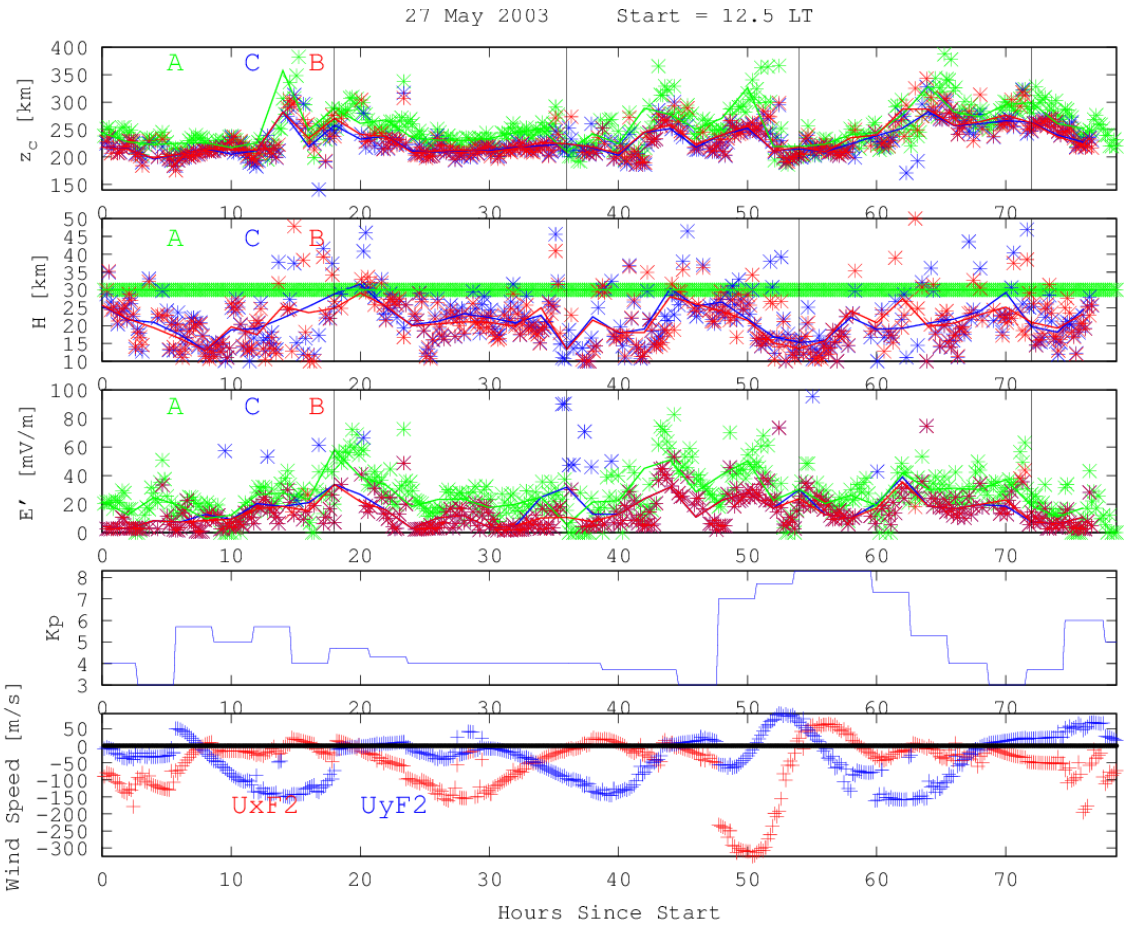

Figure 3.15: Models A, B, and C for the 27 May 2003 storm dataset are juxtaposed along with geomagnetic and neutral wind activity.

latitude daytime and nighttime z_c increases with increased geomagnetic activity.

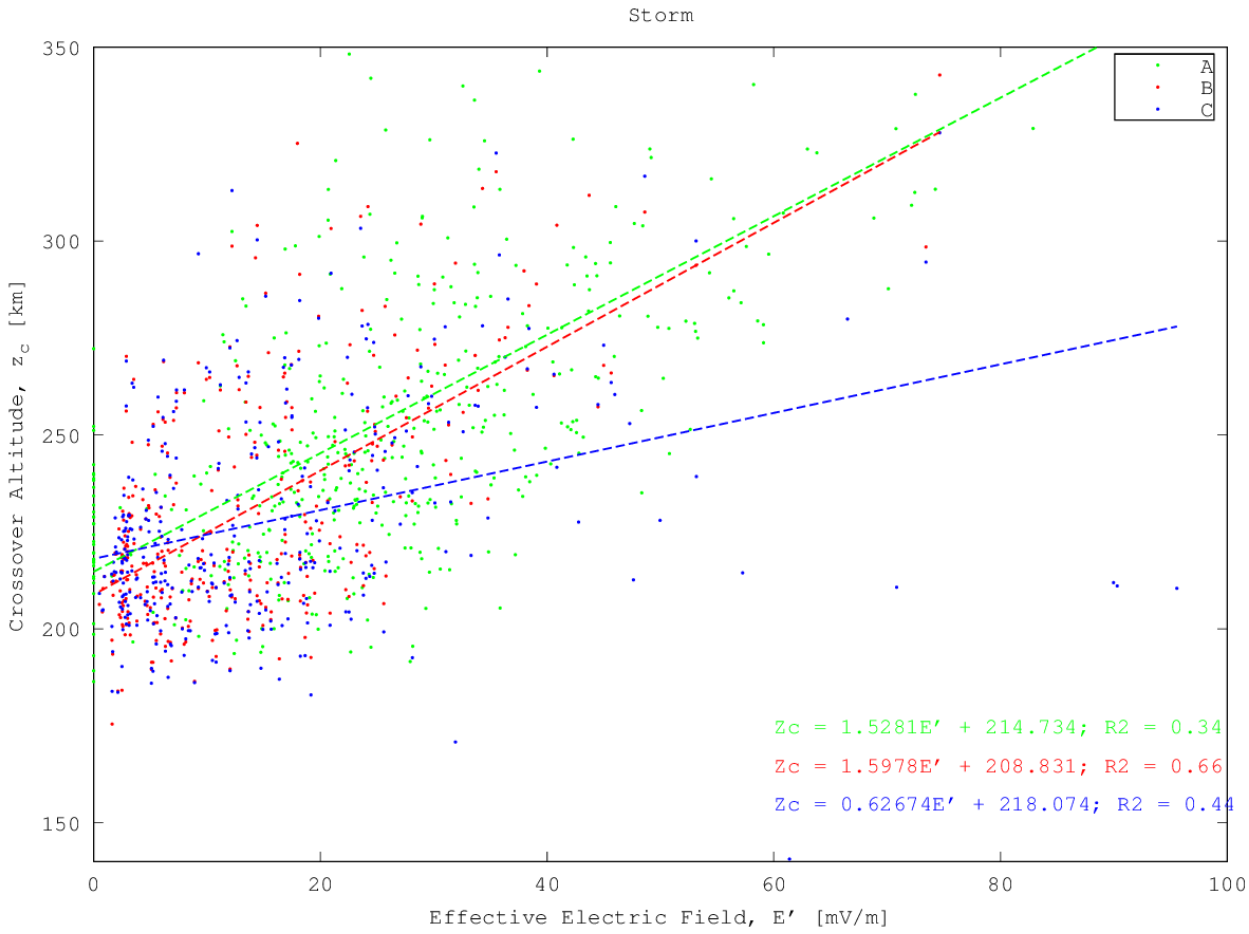

Figure 3.16: The correlation between effective electric field and crossover altitude for the data in Figure 3.15 above.

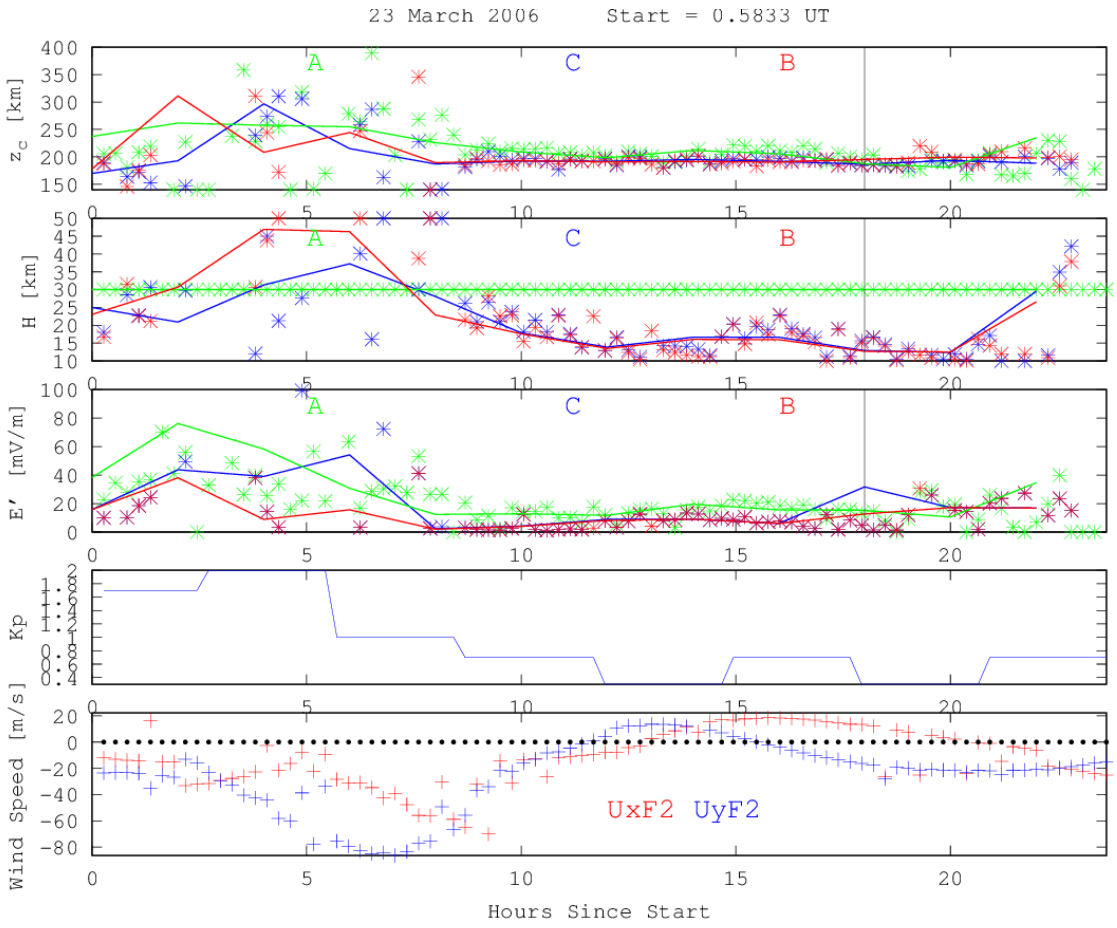

Figure 3.17: Models A, B, and C for the 23 March 2006 quiet dataset are juxtaposed along with geomagnetic and neutral wind activity.

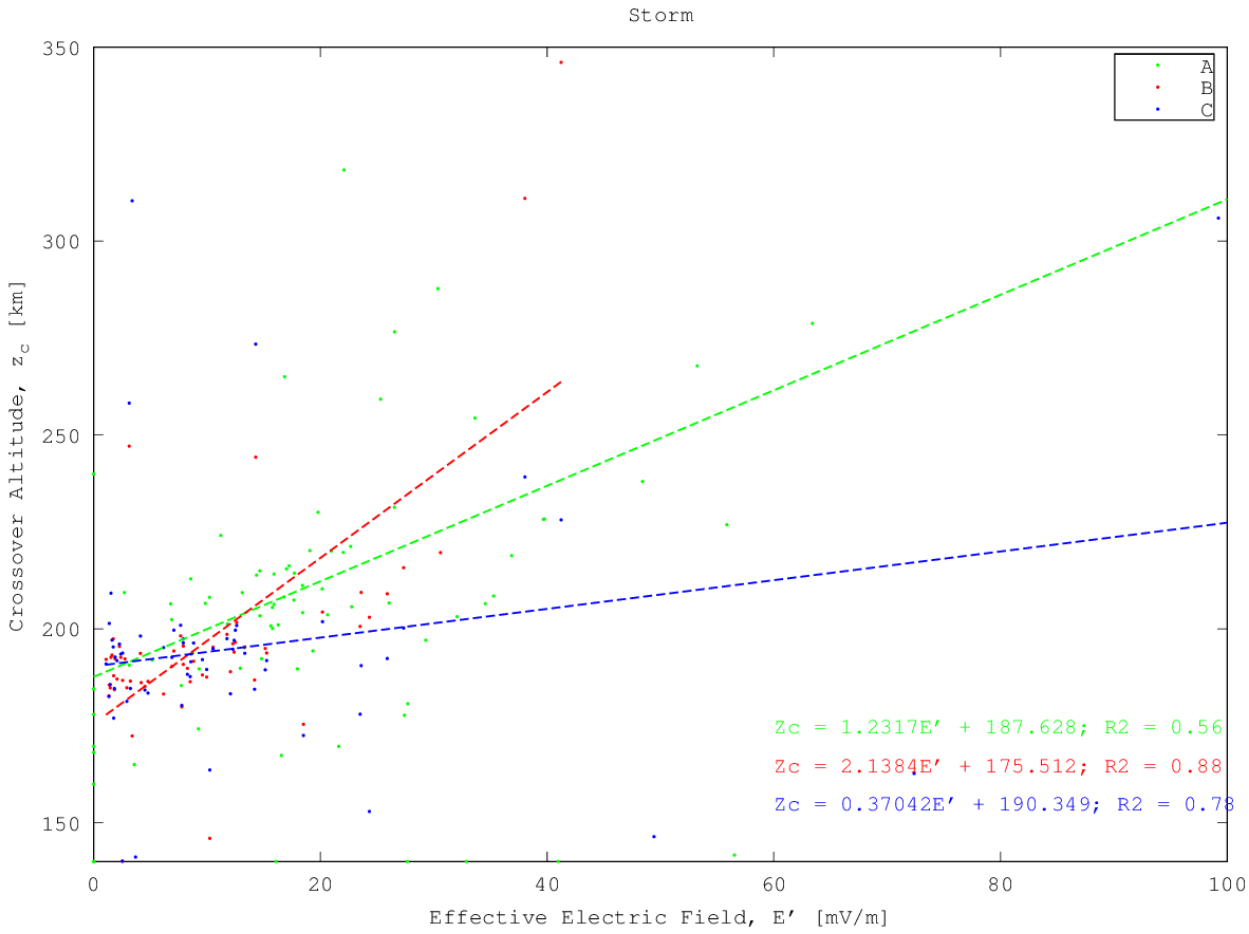

Figure 3.18: The correlation between effective electric field and crossover altitude for the data in Figure 3.17 above.

Chapter 4

Results: Statistical Analysis of Case Studies

In this chapter, the storm and quiet datasets as described in Table 3.1 are combined to create two large datasets, one for storms and one for quiet times.

4.1 Local Time Binning

This section looks at the behaviors of the crossover altitude, scale height, and electric fields as a function of local time (LT) while also considering differences between quiet and storm datasets. The data are aggregated into Figure 4.1 below.

4.1.1 Crossover Altitude

Figures 4.1a and 4.1b show the z_c dependence on local time at Sondrestrom for storm and quiet times, respectively. The average storm z_c value is 242 km (250 km for Model A, 239 km for Model B, and 237 km for Model C). The average quiet z_c value is 200 km (207 km for Model A, 196 km for Model B, and 197 km for Model C). Thus, during geomagnetic storms, there is an average z_c increase of about 40 km, consistent with Litvin et al. [1998]'s findings of mid latitude daytime

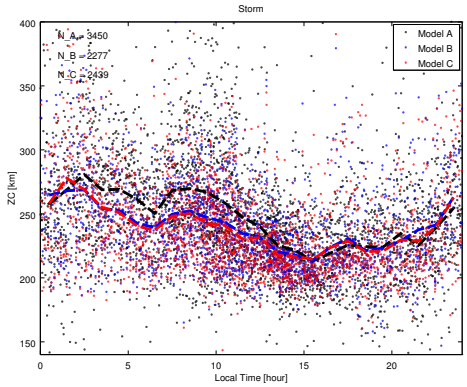

(a) Storm z_c

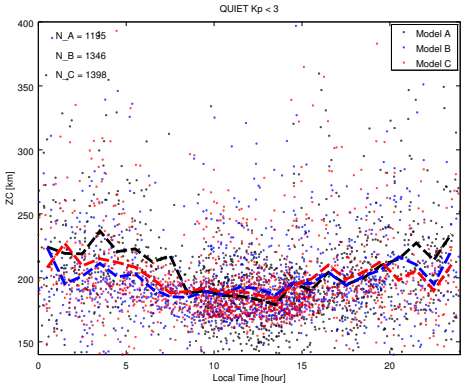

(b) Quiet z_c

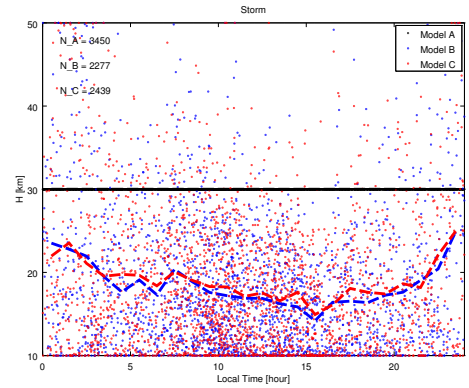

(c) Storm H

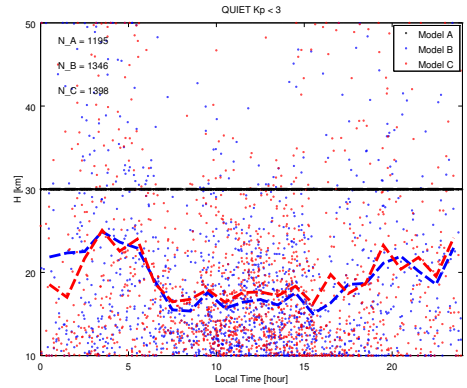

(d) Quiet H

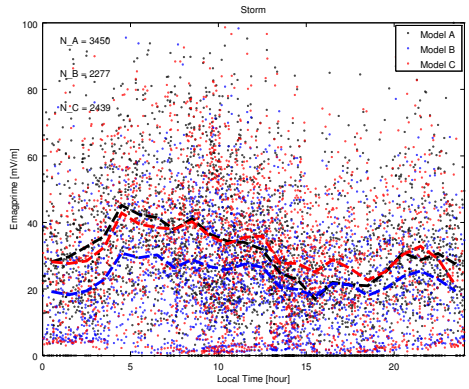

(e) Storm $E'_\perp$

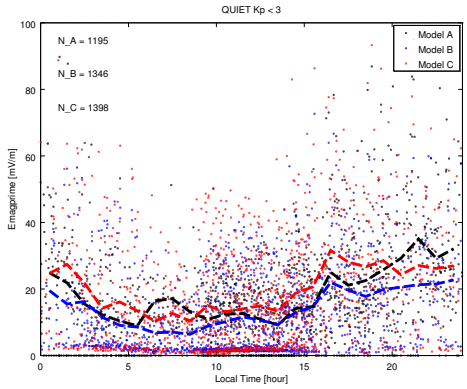

(f) Quiet $E'_\perp$

Figure 4.1: The composition parameters, z_c, H, and $E'_\perp$, for Models A, B, and C, binned by local time. Model A is black, Model B is blue, and Model C is red. Storm data is on the left while quiet data is on the right.

and nighttime z_c increases with increased geomagnetic activity. It is also consistent with Cabrit and Kofman [1997]'s findings of quiet time z_c increases from their statistical analysis of EISCAT data. It is noted, for both quiet and storm times, that Model A shows, on average, larger values for z_c than Models B and C.

The diurnal trends for quiet times show a minimum of 185 km just after sunrise until about 2 pm LT. The crossover altitude then increases to a maximum of about 220 km from midnight to 2 am LT. It then decreases to its minimum at sunrise. Having a minimum mid day and maximum just after midnight (1-2 am LT) is consistent with the general trends found in Lei et al. [2004], Litvin et al. [1998]. Nighttime increases of z_c by more than 20 km are consistent with Litvin et al. [1998].

There are also two peaks in the storm data: one around 2 LT and the other around 8-9 LT. The minimum between these two peaks occurs at sunrise (6-7 LT). This second peak does not occur in the quiet time data. It's suggested that this second peak occurs due to the continued presence of large $E'_\perp$ values (> 30 $^{\mathrm{mV}}/_{\mathrm{m}}$). This is seen in Figures 4.1e and 4.1f: there are large electric field values from 4 am LT to noon in the storm data where as the quiet data has a minimum of electric field values from 3 am to 3 pm LT. At sunrise, the solar flux increases O^+ but the presence of large electric fields cause frictional heating and thus converts the O^+ into NO^+ through the temperature sensitive reaction given in (1.1). Another possibility is that during these geomagnetic storms, the thermosphere increases the $^{\mathrm{N2}}/_{\mathrm{O}}$ ratio, thus increasing the efficiency of Reaction (1.1).

4.1.2 Effective Electric Field

Figures 4.1e and 4.1f show the $E'_\perp$ dependence on local time at Sondrestrom for storm and quiet times, respectively. The average storm $E'_\perp$ value is 30.7 $^{\mathrm{mV}}/_{\mathrm{m}}$ (34.4 $^{\mathrm{mV}}/_{\mathrm{m}}$ for Model A, 23.9 $^{\mathrm{mV}}/_{\mathrm{m}}$ for Model B, and 32.1 $^{\mathrm{mV}}/_{\mathrm{m}}$ for Model C). The average quiet $E'_\perp$ value is 17.7 $^{\mathrm{mV}}/_{\mathrm{m}}$ (22.3 $^{\mathrm{mV}}/_{\mathrm{m}}$ for Model A, 12.8 $^{\mathrm{mV}}/_{\mathrm{m}}$ for Model B, and 18.1 $^{\mathrm{mV}}/_{\mathrm{m}}$ for Model C). Thus, during geomagnetic storms, there is an average $E'_\perp$ increase of about 12 $^{\mathrm{mV}}/_{\mathrm{m}}$. It is noted that for Models B and C, the presented $E'_\perp$ is the average value for all altitudes (100-500 km) since it varies as the wind and

magnetic field vary ($E_\perp$ is constant along the field line). It's also noted that for both storm and quiet times, Model B has smaller values for $E'_\perp$ than Models A or C, discussed further in Section 4.1.4.

The diurnal trends for quiet times show a minimum of 12 (7 for Model B) $^{\mathrm{mV}}/_{\mathrm{m}}$ from sunrise until 2 pm LT. The effective electric field then increases to a local maximum at 4 pm LT following by a short dip and increasing again to a maximum at 1-2 am LT. This is followed by a decrease until the minimum values are hit at sunrise. The diurnal trends for storm times show a minimum of about 25 (20 for Model B) $^{\mathrm{mV}}/_{\mathrm{m}}$ from 3 pm LT until nightfall. There is then a local maximum at 10 pm LT of 33 (25 for Model B) $^{\mathrm{mV}}/_{\mathrm{m}}$. These values then decrease back to the minimum just before midnight. This is followed by a sharp increase back to about 30 $^{\mathrm{mV}}/_{\mathrm{m}}$ followed by increases until a maximum of over 40 $^{\mathrm{mV}}/_{\mathrm{m}}$ is reached between 4-5 am LT. These elevated effective electric field values last until noon LT. From noon to 3 pm LT, the electric field decreases until its minimum is reached. Thus, it is seen that the storm and quiet time $E'_\perp$ diurnal trends are vastly different.

4.1.3 Scale Height

Figures 4.1c and 4.1d show the H dependence on local time at Sondrestrom for storm and quiet times, respectively. Model A uses a constant scale height of 30 km. The average storm H value for Models B and C is 18.8 km (18.5 km for Model B, and 19.0 km for Model C). The average quiet H value for Models B and C is 19.3 km (19.2 km for Model B, and 19.5 km for Model C). Thus, in the average sense, geomagnetic storms do not greatly affect the scale height, the height over which plasma transitions between molecular and atomic ions.

The diurnal trends for scale height follow closely with the crossover altitude diurnal trends. There is a minimum from just after sunrise until 3 pm LT. The scale height then increases to a maximum at 1-2 am LT for storms and at 3-5 am LT for quiet times. Thus, it appears that the influence of the sun causes a smaller scale height.

4.1.4 Model Comparison

From the above figures, some insight into the Models is gleaned. For Models B and C, z_c and H showed no significant differences. However, the $E'_\perp$ for Model B is consistently lower and Models A and C are in agreement. The main difference between Models A and B is the addition of neutral winds from the HWM. How collisions are handled in Model B with the addition of explicitly finding the winds acts to lower $E'_\perp$. However, when a more complete collisional model is used such as the one in Model C, $E'_\perp$ increases back to implicit wind (Model A) levels. Thus, it appears that accounting for Coulomb collisions is important in estimation of $E'_\perp$. Model A instead estimates a larger crossover altitude, thus putting NO^+ higher into the atmosphere.

4.2 Local Time and Kp Binning

This section looks at the behaviors of the crossover altitude, scale height, and electric fields as a function of local time and K_p for the storm data using the different models. The data is first binned into one of three K_p bins: $0 \leq K_p < 3$ or $3 \leq K_p < 6$ or $k_p \geq 6$. The data is then binned into local time by the hour. A summary of these results is presented in Table 4.1.

4.2.1 Model A

Figure 4.2 shows the z_c dependence for Model A as a function of local time for various storm conditions: near storm, storm, and extreme storm. During near storm periods (left panel) z_c averages 225 km with a minimum at nightfall and a maximum around midnight. This is larger than the quiet average of 207 km for Model A. Also, the 1-2 LT peak is the same as the average storm peak as shown in Figure 4.1a. During storm periods (middle and right panel) the z_c average raises to 253km with an additional peak 2-3 hours after sunrise. The overall z_c trend in the left panel is consistent with aggregate quiet dataset data as seen in Figure 4.1b, minus the minimum at 7 pm LT. The storm time z_c trend is consistent with Figure

4.1a. It is also noted that the post sunrise peak is larger than the 1-2 LT peak for extreme storms and vice versa for storms.

Figure 4.3 shows Model A's effective electric fields. There is seen an increase in electric field activity as K_p increases: near storm periods average 20 $^{mV}/_{m}$ (smaller than Model A's average quiet values yet larger than the total average along with Models B and C's averages), storm periods average 30 $^{mV}/_{m}$, and extreme storm periods average 40 $^{mV}/_{m}$. The effective electric field values are minimum in the afternoon, increasing at nightfall until noon for storms and until sunrise for quiet periods. It is postulated that there is a double peak in the z_c storm plot due to this increased electric field activity. The crossover altitude lowers at sunrise due to solar flux but since there are still strong electric fields NO^+ is being created from O^+ through Reaction (1.1), thus increasing z_c again. The near storm and storm trends are consistent with Figures 4.1f and 4.1e minus the quiet spike at noon in Figure 4.3. It is also noted that the near storm, storm, and extreme storm electric field trends follow the midnight to 5 LT trend for storm time electric fields: a minimum at midnight rising to a maximum at 5 LT. This is contrasted with the quiet trend of maximum at midnight-2 LT and falling to a minimum at 5 LT.

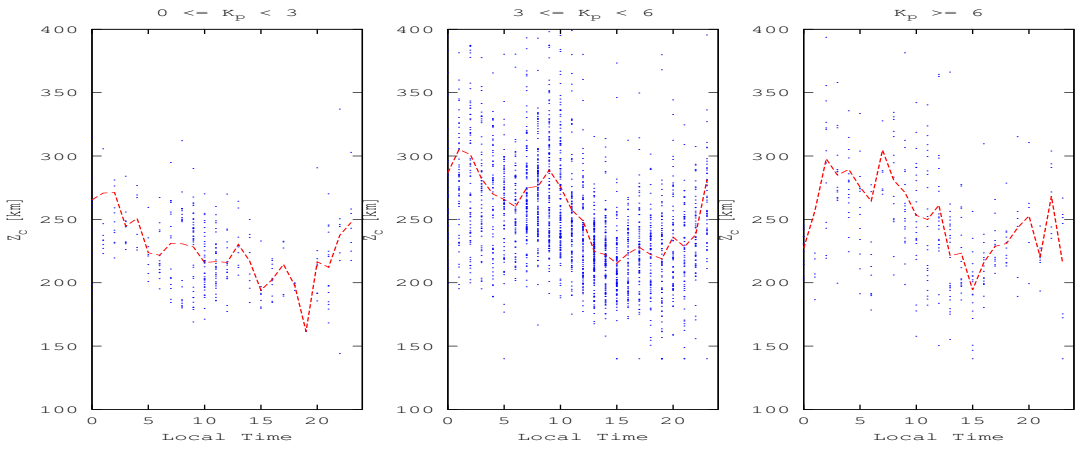

Figure 4.2: Model A's crossover altitude at local times binned into K_p index. The disturbed panels ($K_p \geq 3$)show a z_c enhancement from 20 to 15 LT as compared to the quiet panel ($K_p < 3$).

4.2.2 Model B

Figure 4.4 shows the z_c dependence for Model B as a function of local time for various storm conditions: near storm, storm, and extreme storm.. During all periods, there is a minimum in the afternoon with peaks after midnight and just after sunrise; however, the storm periods see much larger peaks that reach up to 300km while the near storm period peaks stay below about 250 km. The near storm averages are larger than the quiet averages.

From Figure 4.6 below, which looks at Model B's electric fields, there is seen an increase in electric field activity during storms: near storm periods average 20 $^{\mathrm{mV}}/_{\mathrm{m}}$, storm periods average 25 $^{\mathrm{mV}}/_{\mathrm{m}}$, and extreme storm periods average 35 $^{\mathrm{mV}}/_{\mathrm{m}}$, all of which are higher than the quiet and storm averages in the previous section for Model B. For near storm periods, the electric field values are minimum at sunrise with peaks at 4 am LT and nightfall. For storm periods, (middle panel) the electric field values are minimum in the afternoon with a peak following nightfall, then another minimum at midnight, and a maximum from 4 am LT to noon. For extreme storm periods the electric field values see an extreme peak at sunrise and 4 pm LT. Again, it is postulated that there is a large double peak in z_c due to enhanced electric field activity during storms.

Figure 4.5 shows Model B's scale heights for different levels of geomagnetic activity. During near storm periods, there is an increase in scale height around sunrise. During storm periods (middle panel), there is an increase in scale height at midnight and sunrise. During extreme storm periods (right panel), there is an increase in scale height at 2 am LT and 9 am LT with a minimum at sunrise. H being larger at nighttime implies that solar flux lowers H. It also implies that a larger density of O^+ is present at lower altitudes at nighttime than during daytime, if z_c is held constant.

All of the above trends are consistent with Section 4.1 findings and its comparison of quiet versus storm data.

4.2.3 Model C

Figure 4.7 shows the z_c dependence for Model C as a function of local time for various storm conditions: near storm, storm, and extreme storm. During all periods there are minimums in the afternoon. For quiet periods, there is a slight enhancement near sunrise and midnight. For storm and extreme storm periods, there is a double peak in z_c at midnight (1-2 am LT for extreme storms) and 1-2 hours after sunrise. There is a minimum between the peaks which coincides with sunrise. This double peak is postulated to be caused by large electric field values which continue from nighttime through noon as seen in Figure 4.9. There is an average z_c enhancement for increasing geomagnetic activity: 225 km for near storm (27 km larger than the Model C quiet averages), 240 km for storm, and 250 km for extreme storm. There are also electric field enhancements between the storm conditions as seen in Figure 4.9. The scale height, Figure 4.8, follows the trend of getting larger at nighttime. All of the above trends are consistent with Section 4.1 findings and its comparison of quiet versus storm data.

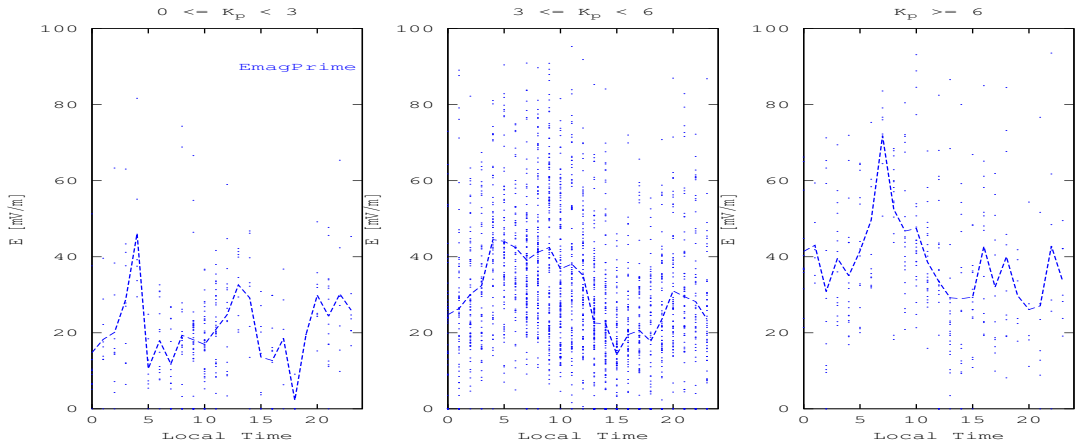

Figure 4.3: Model A's effective electric field at local times binned into K_p index. The disturbed panels ($K_p \geq 3$) show an $E'_\perp$ enhancement from nightfall to noon. The average in the panels from left to right are roughly 20, 30, and 40 mV/m.

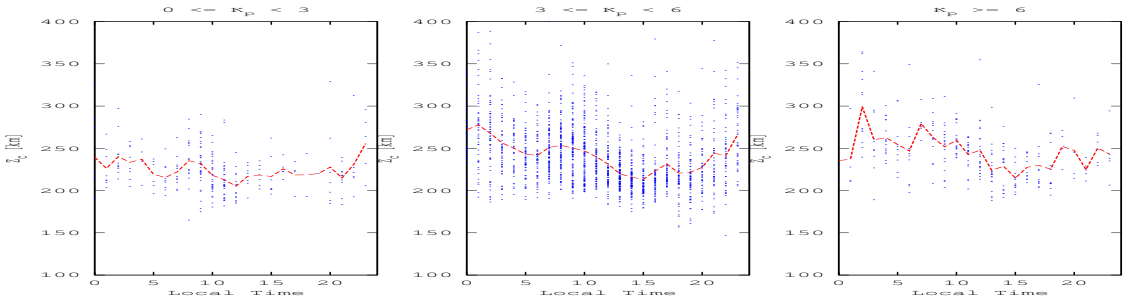

Figure 4.4: Model B's crossover altitude at local times binned into K_p index. The disturbed panels ($K_p \geq 3$) show a z_c enhancement as compared to the quiet panel ($K_p < 3$).

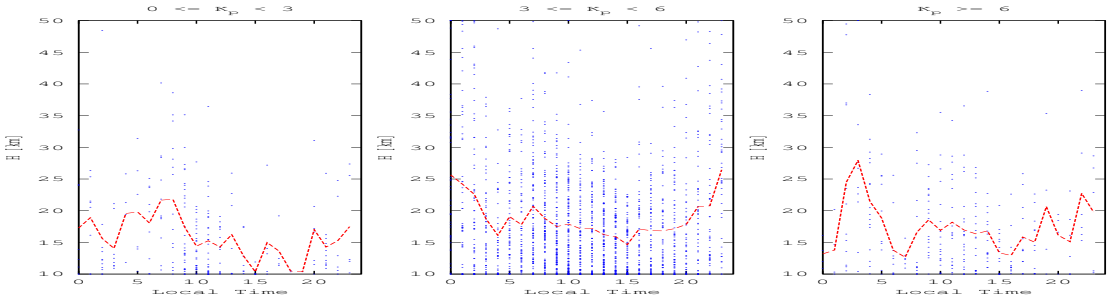

Figure 4.5: Model B's scale height at local times binned into K_p index. The disturbed panels ($K_p \geq 3$) show an overall H enhancement as compared to the quiet panel ($K_p < 3$) with peaks at nighttime.

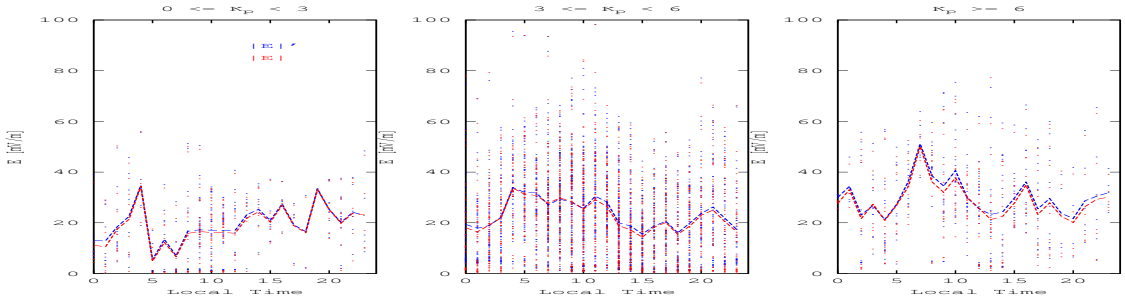

Figure 4.6: Model B's electric and effective electric field at local times binned into K_p index. The disturbed panels ($K_p \geq 3$) show an $E'_{\perp}$ enhancement from nightfall to noon. The average in the panels from left to right are roughly 20, 25, and 35 $^{mV}/_{m}$.

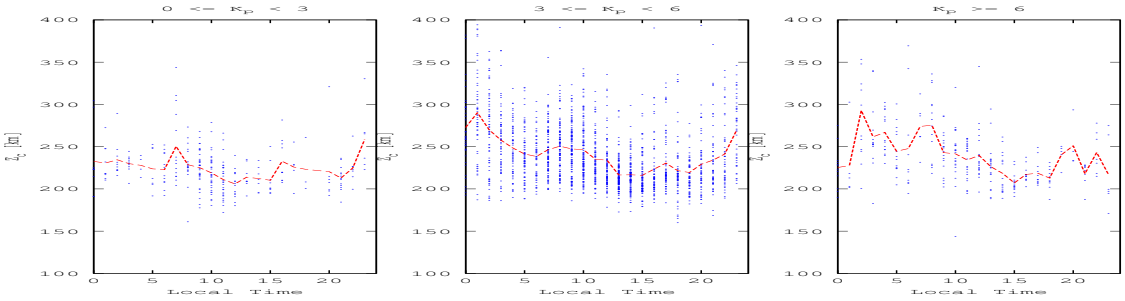

Figure 4.7: Model C's crossover altitude at local times binned into K_p index. The disturbed panels ($K_p \geq 3$) show a z_c enhancement as compared to the quiet panel ($K_p < 3$).

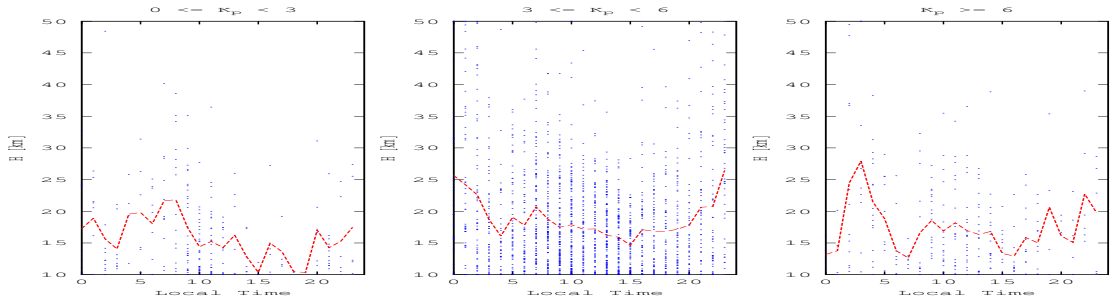

Figure 4.8: Model C's scale height at local times binned into K_p index. The disturbed panels($K_p \geq 3$) show an overall H enhancement as compared to the quiet panel ($K_p < 3$) with peaks at nighttime.

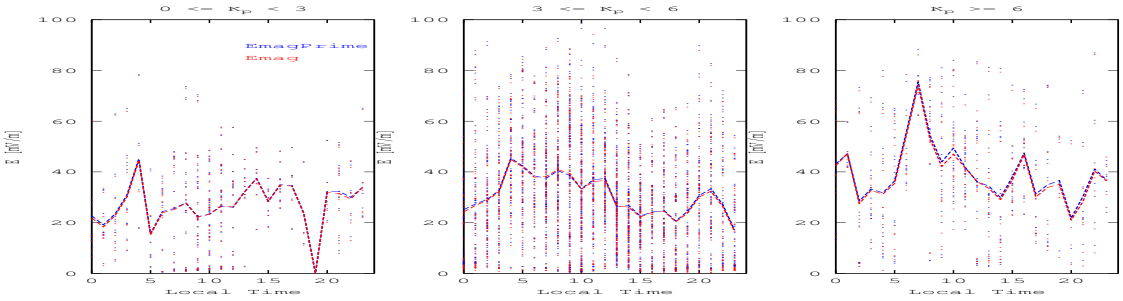

Figure 4.9: Model C's electric and effective electric field at local times binned into K_p index. The disturbed panels ($K_p \geq 3$) show an $E'_{\perp}$ enhancement from nightfall to noon. The average in the panels from left to right are roughly 25, 30, and 40 $^{mV}/_{m}$.

4.3 Transition Altitude Increases Due to Frictional Heating

The below two figures, Figures 4.10a and 4.10b, are a representation of how z_c increases due to frictional heating as portrayed by $E'_\perp$ for storm and quiet times, respectively. In general, all three models agree that transition altitude increases as $E'_\perp$ increases, as expected from the temperature sensitive reaction, (1.1). This is consistent with the modeling work done by Zettergren and Semeter [2012]. It is also seen that there is an increase of z_c of about 40 km regardless of $E'_\perp$ due to geomagnetic activity. This is consistent with Sections 4.1.1 and 4.2 above.

Of note are the slope differences between storms and quiet times. For Models B and C, the slopes during storms are about half those during quiet times. In other words, for every increase of 1 $^{\mathrm{mV}}\!/_{\mathrm{m}}$ the crossover altitude will increase by twice the amount during quiet times as during storms. Thus, it appears easier (from an effective electric field perspective) to move the crossover altitude when the atmosphere is geomagnetically quiet. This trend is not seen in model A. It is noted that there are much fewer data points for $E'_\perp > 50$ $^{\mathrm{mV}}/_{\mathrm{m}}$ for the quiet dataset as compared with the storm dataset.

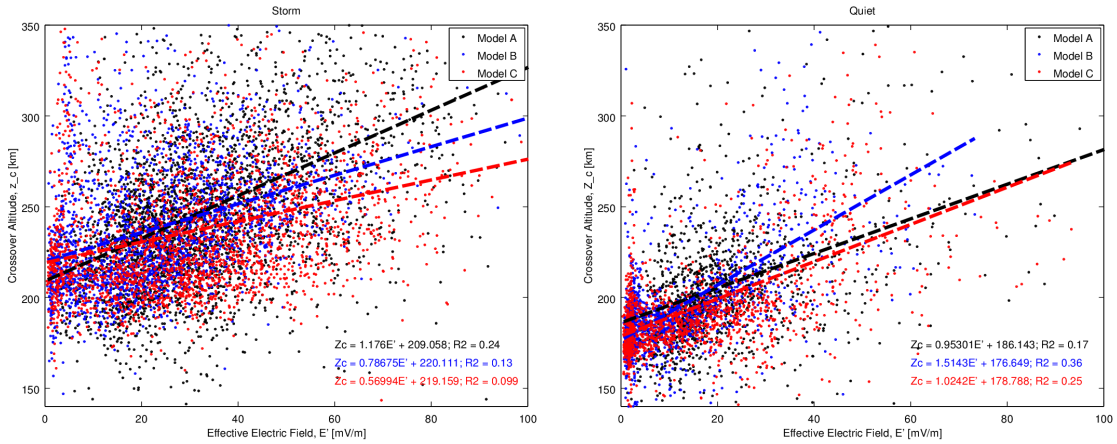

(a) Storm (b) Quiet

Figure 4.10: The effect of the effective electric field on crossover altitude for quiet and storm datasets.

4.4 Geomagnetic Activity Rapid Transitions and Crossover Altitude Disturbances

Rapid K_p transitions of 3 or more can be representative of impulsive energy input into the ionosphere. These events as seen below in Figure 4.11, which uses Model C, lead to increased yet highly variable crossover altitudes. As the crossover altitude increases, NO^+ is found higher into the atmosphere. Following after the nighttime transitions (about 17 and 62 on the x-axis for Figure 4.11 and), z_c increases overall while also varying by 50-100 km every 10 minutes (the timestep). The daytime transition (47-48) occurs during a local minimum about the local time with respect to z_c. The ionosphere appears relatively undisturbed from this transition suggesting that particle flux and/or photoionization dominate in the daytime over any influence these transitions might have. However, about 5 hours after this daytime transition, z_c is lower by over 50 km.

Figure 4.12 is a dataset from 11 November 2003 that shows Model C's z_c calculations along with K_p as time progresses. K_p transitions are seen at nightfall (about 10 and 33) that see a z_c increase along with large variation of over 50 km between

time steps. The K_p transitions at sunrise (93) is followed by a decrease in z_c and then an increase in z_c with variations between the timesteps on the order of 50 km. Although there does seem to be correlation between these transitions and z_c, this dataset's transitions often occur during sunrise or nightfall, which have strong diurnal trends, as shown earlier in this chapter. A more systematic analysis of rapid K_p transitions needs to be done in order to draw confident conclusions.

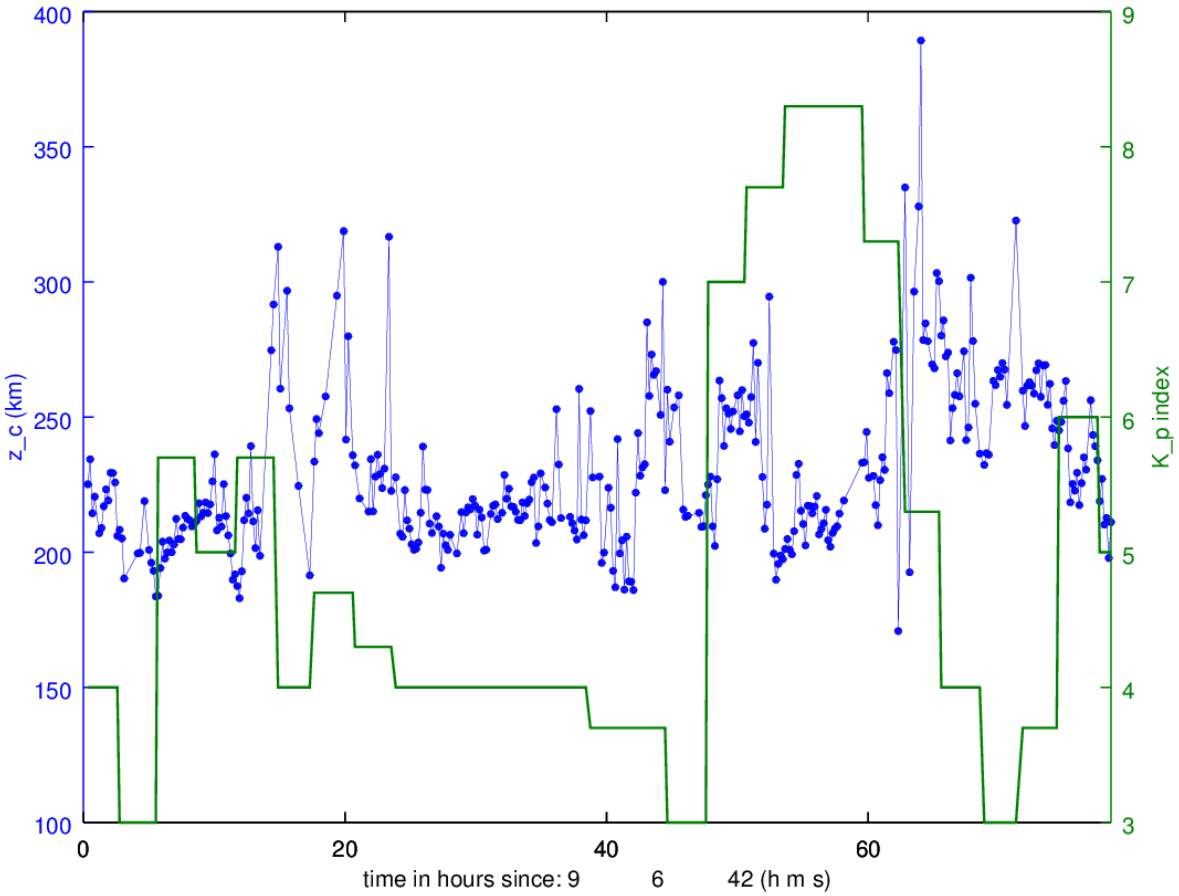

Figure 4.11: K_p and z_c throughout the storm of 27 May 2003. There is a large amount of z_c variation near large K_p transitions.

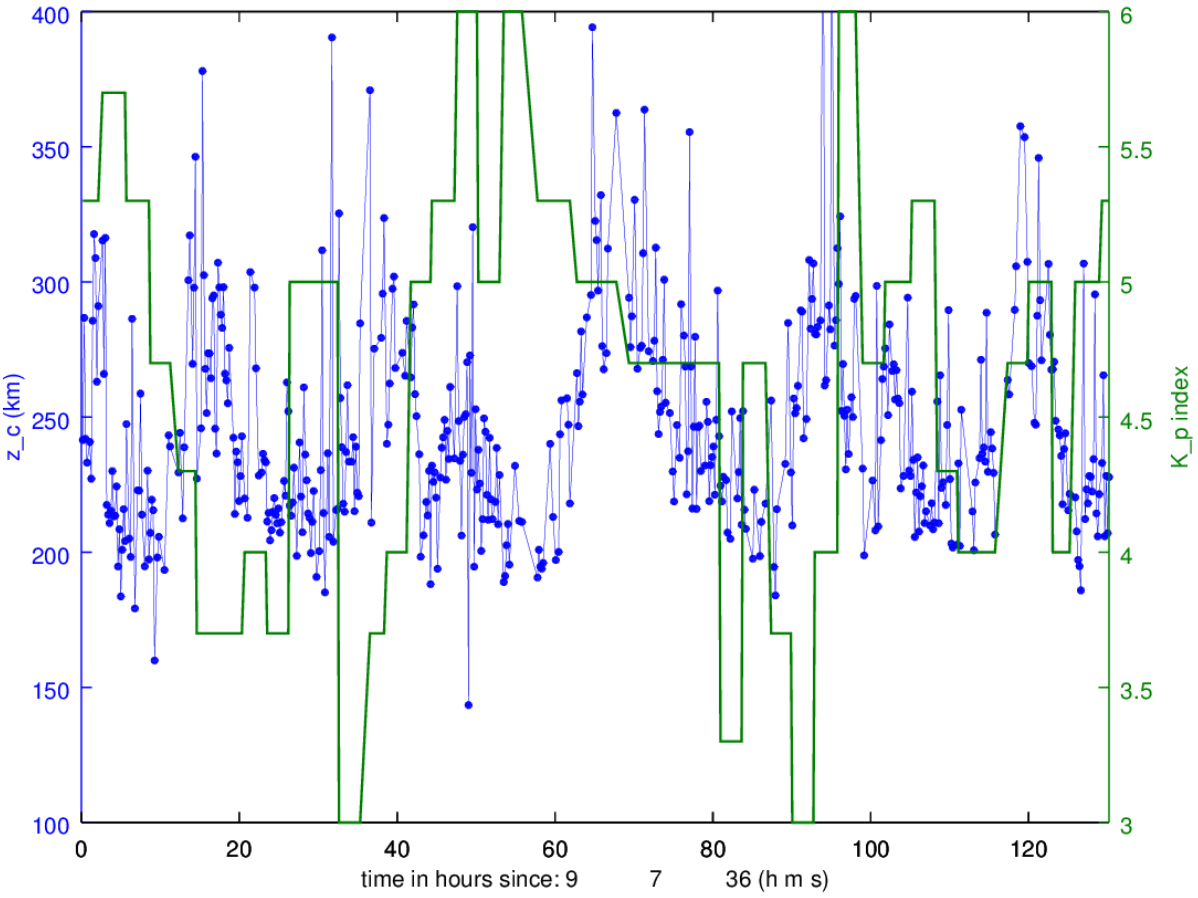

Figure 4.12: K_p and z_c throughout the storm of 11 November 2003. There is a large amount of z_c variation near large K_p transitions.

4.5 Summary of Average Results

This section presents the averages of this chapters results for quiet and storm times for Models A, B, and C in Table 4.1 below.

Average Estimation Parameters

			Model A			Model B			Model C		
Average	Quiet*	Storm*	NS	S	ES	NS	S	ES	NS	S	ES
z_c [km]	200	242	226	255	251	225	242	246	225	242	239
H^* [km]	19.3	18.8	30	30	30	15.9	18.9	17.4	15.9	18.9	17.4
$E'_\perp$ [mV/m]	17.7	30.7	21.1	30.4	38.9	19.6	23.5	30.2	27.2	30.9	40.0

Table 4.1: The average values of $\boldsymbol{x}_{est}$ for each Model for different geomagnetic conditions. NS, S, and ES, stand for near storm, storm, and extreme storm, respectively, as defined in Section 4.2. H averages do not include Model A as it assumed constant at 30 km. Quiet and Storm averages include all 3 models.

Chapter 5

Conclusions and Future Work

5.1 Conclusions

This work has presented an approach to account for dynamic (<1 minute) ion composition variation in the ionosphere, specifically at high latitudes for which the temperature-mass ambiguities of ISR data exists. A comparison with previous work performed in Zettergren et al. [2011] is done with two new methods, henceforth called Models B and C, of computing ion composition that incorporate altitude-dependent neutral winds, variable scale height, and simultaneous parameter estimation. Model C uses a more thorough accounting of collisions, including Coulomb collisions which are not included in the other methods. This is done using the 13-moment approximation to the transport equations of multi-species flows [Schunk, 1977].

Several ISR datasets were used to conduct the presented analysis, including storm time datasets where $K_p \geq 4$ for at least 4 hours, and quiet time datasets where $K_p < 3$ for all times. The differences in how the three models fit temperature profiles to the radar temperature profile is presented and used to suggest that Model C, which incorporates the most realistic collisional model, performs the most realistically. Also discussed were the effects of implicitly or explicitly including the neutral winds in the analysis and the effect of sequential or simultaneous

estimation of ion composition parameters. It was shown that implicit wind estimation leads to higher estimates of z_c, H, and $E'_\perp$. It was also shown that sequential estimation leads to higher estimates of z_c and $E'_\perp$. All three models successfully accounted for frictional heating events, to some degree, as seen by correction of unphysical ISR temperature profile inversions in the F1 region. Results suggest that accounting for Coulomb collisions is important in the estimation of $E'_\perp$.

A statistical analysis was performed by combining all the storm time ISR datasets and all the quiet time ISR datasets to create 2 large datasets representative of storm and quiet times at Sondrestrom. This analysis showed quiet time z_c diurnal trends consistent with previous modeling [Lei et al., 2004] and observational work [Litvin et al., 1998]: z_c is a minimum around noon and a maximum 1-2 hours after midnight. Also seen was an average z_c increase of 40 km between quiet and storm times. The scale height follows a diurnal trend that is similar for quiet and storm conditions: minimum during daytime and quickly rising at nighttime to a maximum. The effective electric field follows a diurnal trend similar to that of z_c with an average difference between storm and quiet times of 12 $^{\mathrm{mV}}/_{\mathrm{m}}$. This relationship between $E'_\perp$ and z_c is intuitive because $E'_\perp$ is responsible for frictional heating, thus producing more NO^+, and raising z_c. It was seen that the storm and quiet time $E'_\perp$ diurnal trends are vastly different.

Also of note was a double peak of z_c during storm times. There is a peak from 1-2 am LT and another one following the decrease at sunrise. This second peak is not seen in the quiet time data. It is postulated that this second peak is due to the sustained increased effective electric field values from 4 am LT to noon during storm times that are not seen in quiet time data. These electric fields quickly heat more moleculars after a steady-state is obtained (the sudden appearance of the sun temporarily alters chemical balance). Another postulated cause of this second peak is that the $^{\mathrm{N2}}/_{\mathrm{O}}$ ratio increases due to thermospheric storms.

5.2 Limitations and Future Work

The work presented in this thesis is limited to the study of field aligned datasets for which a steady-state, collisional model of the ionosphere is valid. Other limitations include the lack of a neutral wind model that includes height, seasonal, and solar activity dependencies for the disturbance wind along with solar activity dependencies for the quiet wind. Future work includes: expansion of algorithms to multi-beam and non-field aligned datasets, such as AMISR; incorporation of a more complete model of the neutral winds, specifically one that includes solar activity dependencies, or FPI data; a statistical analysis of the effects of K_p shocks on crossover altitude while making sure crossover altitude variations are not due to the diurnal trends observed in this work and others; the creation of synthetic datasets to more clearly see how the models react to various conditions; an EISCAT case study. A question that needs to be answered is, what causes the crossover altitude increase after sunrise for storm time data? Is it a thermospheric effect? Is it due to large storm time electric fields? What are the effects of electron precipitation? What does a comparison to TRANSCAR models show? How does ion composition vary spatially? Evidence of this spatial variation is seen in Zettergren et al. [2014] which used a photochemistry model for ion composition from Richards et al. [2010]. Further study of the storm diurnal trends should include ion and neutral density calculations in order to better understand H trends and the z_c double peak.

Bibliography

H. Akbari, J. L. Semeter, H. Dahlgren, M. Diaz, M. Zettergren, A. StrÃ¸mme, M. J. Nicolls, and C. Heinselman. Anomalous isr echoes preceding auroral breakup: Evidence for strong langmuir turbulence. *Geophys. Res. Lett.*, 39, 2012. doi: 10.1029/2011GL050288.

PL Blelly, A Robineau, J Lilensten, and D Lummerzheim. 8-moment fluid models of the terrestrial high latitude ionosphere between 100 and 3000 km. *Solar terrestrial energy program (STEP): handbook of ionospheric models*, pages 53–72, 1996.

B Cabrit and W Kofman. Ionospheric composition measurement by eiscat using a global fit procedure. In *Annales Geophysicae*, volume 14, pages 1496–1505. Springer, 1997.

P-Y Diloy, A Robineau, J Lilensten, P-L Blelly, and J Fontanari. A numerical model of the ionosphere, including the e-region above eiscat. In *Annales Geophysicae*, volume 14, pages 191–200. Springer, 1996.

J. P. Dougherty and D. T. Farley. A Theory of Incoherent Scattering of Radio Waves by a Plasma. *Royal Society of London Proceedings Series A*, 259:79–99, November 1960. doi: 10.1098/rspa.1960.0212.

D. P. Drob, J. T. Emmert, G. Crowley, J. M. Picone, G. G. Shepherd, W. Skinner, P. Hays, R. J. Niciejewski, M. Larsen, C. Y. She, J. W. Meriwether, G. Hernandez, M. J. Jarvis, D. P. Sipler, C. A. Tepley, M. S. O'Brien, J. R. Bowman, Q. Wu, Y. Murayama, S. Kawamura, I. M. Reid, and R. A. Vincent. An empirical model of the earth's horizontal wind fields: Hwm07. *Journal of Geophysical Research:*

Space Physics, 113(A12), 2008. ISSN 2156-2202. doi: 10.1029/2008JA013668. URL http://dx.doi.org/10.1029/2008JA013668.

J.V. Evans. Theory and practice of ionosphere study by thomson scatter radar. *Proceedings of the IEEE*, 57(4):496–530, April 1969. ISSN 0018-9219. doi: 10.1109/PROC.1969.7005.

D. T. Farley. Incoherent scatter correlation function measurements. *Radio Science*, 4 (10):935–953, 1969. ISSN 1944-799X. doi: 10.1029/RS004i010p00935. URL http://dx.doi.org/10.1029/RS004i010p00935.

C. C. Finlay, S. Maus, C. D. Beggan, T. N. Bondar, A. Chambodut, T. A. Chernova, A. Chulliat, V. P. Golovkov, B. Hamilton, M. Hamoudi, R. Holme, G. Hulot, W. Kuang, B. Langlais, V. Lesur, F. J. Lowes, H. Lühr, S. MacMillan, M. Mandea, S. McLean, C. Manoj, M. Menvielle, I. Michaelis, N. Olsen, J. Rauberg, M. Rother, T. J. Sabaka, A. Tangborn, L. Tøffner-Clausen, E. Thébault, A. W. P. Thomson, I. Wardinski, Z. Wei, and T. I. Zvereva. International Geomagnetic Reference Field: the eleventh generation. *Geophysical Journal International*, 183:1216–1230, December 2010. doi: 10.1111/j.1365-246X.2010.04804.x. URL http://adsabs.harvard.edu/abs/2010GeoJI.183.1216F. Provided by the SAO/NASA Astrophysics Data System.

P Gaimard, C Lathuillere, and D Hubert. Non-maxwellian studies in the auroral f region: a new analysis of incoherent scatter spectra. *Journal of Atmospheric and Terrestrial Physics*, 58(1):415–433, 1996.

P Gaimard, J-P St-Maurice, C Lathuillere, and D Hubert. On the improvement of analytical calculations of collisional auroral ion velocity distributions using recent monte carlo results. *Journal of Geophysical Research: Space Physics (1978–2012)*, 103(A3):4079–4095, 1998.

Tor Hagfors. Density fluctuations in a plasma in a magnetic field, with applications to the ionosphere. *Journal of Geophysical Research*, 66(6):1699–1712, 1961. ISSN

2156-2202. doi: 10.1029/JZ066i006p01699. URL http://dx.doi.org/10.1029/JZ066i006p01699.

D Hubert and C Lathuillere. Incoherent scattering of radar waves in the auroral ionosphere in the presence of high electric fields, and measurement problems with the eiscat facility. *Journal of Geophysical Research: Space Physics (1978–2012)*, 94(A4):3653–3662, 1989.

B. Jenkins, R. J. Moffett, J. A. Davies, and M. Lester. Nightside ion frictional heating: atomic and molecular ion temperature anisotropy and ion composition changes. *Journal of Atmospheric and Solar-Terrestrial Physics*, 59:1329–1341, July 1997. doi: 10.1016/S1364-6826(96)00019-3. URL http://adsabs.harvard.edu/abs/1997JASTP..59.1329J. Provided by the SAO/NASA Astrophysics Data System.

C. Lathuillere, G. Lejeune, and W. Kofman. Direct measurements of ion composition with EISCAT in the high-latitude F1 region. *Radio Science*, 18:887–893, December 1983. doi: 10.1029/RS018i006p00887.

J. Lei, L. Liu, W. Wan, and S.-R. Zhang. Model results for the ionospheric lower transition height over mid-latitude. *Annales Geophysicae*, 22(6):2037–2045, 2004. doi: 10.5194/angeo-22-2037-2004. URL http://www.ann-geophys.net/22/2037/2004/.

A. Litvin, W. Kofman, and B. Cabrit. Ion composition measurements and modelling at altitudes from 140 to 350 km using eiscat measurements. *Annales Geophysicae*, 16(10):1159–1168, 1998. doi: 10.1007/s00585-998-1159-6. URL http://www.ann-geophys.net/16/1159/1998/.

IW McCrea, M Lester, TR Robinson, J-P St-Maurice, NM Wade, and TB Jones. Derivation of the ion temperature partition coefficient βâˆ¥ from the study of ion frictional heating events. *Journal of Geophysical Research: Space Physics (1978–2012)*, 98(A9):15701–15715, 1993.

M. McFarland, D. L. Albritton, F. C. Fehsenfeld, E. E. Ferguson, and A. L. Schmeltekopf. Flow-drift technique for ion mobility and ion-molecule reaction rate constant measurements. II. Positive ion reactions of N^+, O^+, and H^+_2 with O_2 and O^+ with N_2 from thermal to [inverted lazy s]2 eV. *Journal of Chemical Physics*, 59:6620–6628, December 1973. doi: 10.1063/1.1680042.

D. R. Moorcroft. On the determination of temperature and ionic composition by electron backscattering from the ionosphere and magnetosphere. *Journal of Geophysical Research*, 69(5):955–970, 1964. ISSN 2156-2202. doi: 10.1029/JZ069i005p00955. URL `http://dx.doi.org/10.1029/JZ069i005p00955`.

Thomas E Moore and JL Horwitz. Stellar ablation of planetary atmospheres. *Reviews of Geophysics*, 45(3), 2007.

W. L. Oliver. Models of F1-region ion composition variations. *Journal of Atmospheric and Terrestrial Physics*, 37:1065–1076, August 1975. URL `http://adsabs.harvard.edu/abs/1975JATP...37.1065O`. Provided by the SAO/NASA Astrophysics Data System.

W. L. Oliver. Incoherent scatter radar studies of the daytime middle thermosphere. *Annales de Geophysique*, 35:121–139, September 1979.

R. S. Venkat Raman, J. P. St-Maurice, and R. S. B. Ong. Incoherent scattering of radar waves in the auroral ionosphere. *Journal of Geophysical Research: Space Physics*, 86(A6):4751–4762, 1981. ISSN 2156-2202. doi: 10.1029/JA086iA06p04751. URL `http://dx.doi.org/10.1029/JA086iA06p04751`.

P. G. Richards, D. Bilitza, and D. Voglozin. Ion density calculator (idc): A new efficient model of ionospheric ion densities. *Radio Science*, 45(5):n/a–n/a, 2010. ISSN 1944-799X. doi: 10.1029/2009RS004332. URL `http://dx.doi.org/10.1029/2009RS004332`.

J.-P. Saint Maurice and D. G. Torr. Nonthermal rate coefficients in the ionosphere - The reactions of O/+/ with N2, O2, and NO. *Journal of Geophysical Research*, 83:969–977, March 1978. doi: 10.1029/JA083iA03p00969.

R. W. Schunk. Mathematical structure of transport equations for multispecies flows. *Reviews of Geophysics*, 15(4):429–445, 1977. ISSN 1944-9208. doi: 10.1029/RG015i004p00429. URL http://dx.doi.org/10.1029/RG015i004p00429.

R. W. Schunk, W. J. Raitt, and P. M. Banks. Effect of electric fields on the daytime high-latitude e and f regions. *Journal of Geophysical Research*, 80(22):3121–3130, 1975. ISSN 2156-2202. doi: 10.1029/JA080i022p03121. URL http://dx.doi.org/10.1029/JA080i022p03121.

R.W. Schunk and A. Nagy. *Ionospheres: Physics, Plasma Physics, and Chemistry*. Cambridge atmospheric and space science series. Cambridge University Press, 2000. ISBN 9780521632379. URL http://books.google.com/books?id=sBpaHlSxkF4C.

T. Shibata, H. Matsuya, and J. Hoashi. Ion Composition in the Auroral Lower F-Region Inferred from Residuals of Ion Temperature Profiles Observed with EISCAT. *Advances in Space Research*, 25:201–210, 2000. doi: 10.1016/S0273-1177(99)00919-9.

J.-P. St.-Maurice and P. J. Laneville. Reaction rate of o+ with o2, n2, and no under highly disturbed auroral conditions. *Journal of Geophysical Research: Space Physics*, 103(A8):17519–17521, 1998. ISSN 2156-2202. doi: 10.1029/98JA01387. URL http://dx.doi.org/10.1029/98JA01387.

J.-P. St.-Maurice, C. Cussenot, and W. Kofman. On the usefulness of e region electron temperatures and lower f region ion temperatures for the extraction of thermospheric parameters: a case study. *Annales Geophysicae*, 17(9):1182–1198, 1999. doi: 10.1007/s00585-999-1182-2. URL http://www.ann-geophys.net/17/1182/1999/.

Marsha R. Torr, J. P. St. Maurice, and D. G. Torr. The rate coefficient for the o+ + n2 reaction in the ionosphere. *Journal of Geophysical Research*, 82(22):3287–3290, 1977. ISSN 2156-2202. doi: 10.1029/JA082i022p03287. URL http://dx.doi.org/10.1029/JA082i022p03287.

P. Waldteufel. Combined incoherent-scatter f1-region observations. *Journal of Geophysical Research*, 76(28):6995–6999, 1971. ISSN 2156-2202. doi: 10.1029/JA076i028p06995. URL http://dx.doi.org/10.1029/JA076i028p06995.

E. Winkler, J. P. St-Maurice, and A. R. Barakat. Results from improved monte carlo calculations of auroral ion velocity distributions. *Journal of Geophysical Research: Space Physics*, 97(A6):8399–8423, 1992. ISSN 2156-2202. doi: 10.1029/91JA03104. URL http://dx.doi.org/10.1029/91JA03104.

M Zettergren and J Semeter. Ionospheric plasma transport and loss in auroral downward current regions. *Journal of Geophysical Research: Space Physics (1978–2012)*, 117(A6), 2012.

M Zettergren, J Semeter, B Burnett, W Oliver, C Heinselman, P-L Blelly, and M Diaz. Dynamic variability in f-region ionospheric composition at auroral arc boundaries. In *Annales Geophysicae*, volume 28, pages 651–664. Copernicus GmbH, 2010.

M. Zettergren, J. Semeter, C. Heinselman, and M. Diaz. Incoherent scatter radar estimation of f region ionospheric composition during frictional heating events. *Journal of Geophysical Research: Space Physics*, 116(A1), 2011. ISSN 2156-2202. doi: 10.1029/2010JA016035. URL http://dx.doi.org/10.1029/2010JA016035.

M. Zettergren, K. Lynch, D. Hampton, M. Nicolls, B. Wright, M. Conde, J. Moen, M. Lessard, R. Miceli, and S. Powell. Auroral ionospheric f region density cavity formation and evolution: Mica campaign results. *Journal of Geophysical Research: Space Physics*, 119(4):3162–3178, 2014. ISSN 2169-9402. doi: 10.1002/2013JA019583. URL http://dx.doi.org/10.1002/2013JA019583.

M. D. Zettergren. *Model-based optical and radar remote sensing of transport and composition in the auroral ionosphere*. PhD thesis, Boston University, 2009.